

博士論文（要約）

Infrared spectroscopy of water during
adsorption and desorption processes in
metal-organic frameworks

（金属有機構造体の吸着及び脱着過程における水の
赤外分光分析）

高 嬌

Infrared spectroscopy of water during adsorption and desorption processes in metal-organic frameworks

(金属有機構造体の吸着及び脱着過程における水の
赤外分光分析)

高 嬌

Jiao GAO

Department of Mechanical Engineering

The University of Tokyo

Associate Professor Jean-Jacques Delaunay, Supervisor

June 2021

Abstract

Water phases and dynamic behaviors in metal-organic frameworks

By

GAO Jiao

Cooling is one of the most energy-consuming aspects of our modern life. According to the International Energy Agency, the use of air conditioners (AC) and electric fans to stay cool currently account for more than 10% of the total electricity used in housing around the world. In 2050, the energy demand for space cooling is expected to increase to around 37%, which is almost three times than today. The increased use of the conventional AC units will be harmful to the environment, as the flammable and toxic hydrogenated chlorofluorocarbons are always used as refrigerants. Moreover, more electricity will be consumed with the increased AC units, resulting in more CO₂ emissions to the atmosphere.

Recently, due to the potential of high refrigeration efficiency and energy efficient property, the sorption-desorption cycle of water on porous materials is being considered as the cutting-edge replacement for the conventional compression-evaporation cycle used in the air-conditioning systems. In the sorption-desorption cycle, evaporation of the water is induced by the adsorption of porous adsorbent material, and this endothermic process is used to achieve the desired refrigeration effect. Noticeably, for the sorption-based AC units, the property of porous adsorbent and the interaction with adsorbed water molecules

are the crucial factors to the whole system performance and energy consumption, thus becoming the focus of studies and have been widely discussed.

Zeolites and silica gel are two commercial porous materials commonly used in the sorption-based AC units. However, these two adsorbents are not so ideal for this application. For zeolites, a strong interaction between the structures and water molecules is always formed, and therefore a high driving temperature ($> 150^{\circ}\text{C}$) is needed when water is desorbed from the material. With this high driving temperature, the desired low-grade energy sources cannot be used. For silica gel, it processes an unwanted linear shape water isotherm, limiting the exchangeable amount of water in the cycle and the refrigeration efficiency of the whole system. To address the problems of these two adsorbents, activation treatment, acid treatment, and some other methods are always used, which are time and energy-consuming. New energy-saving porous materials must be developed.

Lately, metal-organic frameworks (MOFs) are proposed and have become widely studied as candidates for separation processes, catalytic processes, and gas storage due to their peculiar coordination structures, controllable organic ligands, tailor-made porous morphologies, and large Langmuir surface areas. For metal-organic frameworks, metal means the metal sites, and organic means the organic ligands. The combination of different metal sites and organic ligands forms these MOFs materials with various cages structures and cages properties. As the potential materials used in the sorption-based AC units, the water uptake capacities of different MOFs have been researched, and among all these materials, a MOF called MIL-101(Cr) is the most attractive. This chromium terephthalate-based solid is unique in terms of hierarchical cages with large diameters of

29 Å and 34 Å (window aperture of 12 Å and 16 Å), and corresponding huge pore volume of 12,700 Å³ and 20,600 Å³. Moreover, MIL-101(Cr) possesses high hydrothermal stability that can retain structural integrity up to 240°C, which is higher than other similar porous materials, implying that this material is more suitable for hydrothermal applications. Based on these physical properties, MIL-101(Cr) is the most potential material to become an ideal porous adsorbent used in the sorption-based AC units.

The sorption-desorption property of water adsorbed in the MIL-101(Cr) has been discussed. However, among these current studies, researchers mainly focus on how to enhance the water adsorption property of the MIL-101(Cr) and how to reduce the energy requirement in the desorption process by adding various functional groups, optimizing the pore structures, and adjusting the component elements. Although directly improving the performance is essential, the research of the water sorption-desorption mechanism of the MIL-101(Cr), especially the dynamic phase transitions of water molecules confined in the cages, is also an indispensable part that needs to be comprehensively analyzed not only for its real industrial applications but also for the further development of superior materials used in the sorption-based AC units.

In this thesis, MIL-101(Cr) and two functional MIL-101(Cr) are prepared using a scaled-up version of the reported hydrothermal reaction. The synthesized MIL-101(Cr) is a solid material that has a regular octahedral structure with smooth surfaces. The XRD patterns of it are in good agreement with the previous reports and simulation, indicating that the desired structure of the MIL-101(Cr) is formed. Four characteristic peaks in the Raman spectrum are observed, which are consistent with the previous reports, confirming that the MIL-101(Cr) crystallite is successfully synthesized. For N₂ adsorption isotherm,

as expected, MIL-101(Cr) processes two size cages with the diameter of 2.6 and 3.2 nm in the structures, and it exhibits a large pore volume equals to $2.9 \text{ cm}^3/\text{g}$ with a specific surface area equals to $3601 \text{ m}^2/\text{g}$. In the type-V water isotherm, a significant water adsorption/desorption occurs in a stepwise manner within a narrow pressure variation range in both the adsorption and desorption processes. The total water uptake is 1.3 g/g , which is 2.5 to 5 times higher than that of the zeolites and silica gel. The narrow stepwise sorption manner and superior water uptake indicate that the demand for energy-saving and efficiency improvement could be satisfied using the MIL-101(Cr) as the sorption-desorption material.

Instead of conventional infrared transmission and adsorption spectroscopy, diffuse reflectance infrared spectroscopy (DRIFTS), which can carry more information of the powdered analytes and determine their polymorphic forms, is selected to be used. The phases and transitions of water molecules in the MIL-101(Cr) and two functional MIL-101(Cr) as a function of water amount are elucidated in detail. To further understand the relationship between the water molecules and the MIL-101(Cr) as well as functional MIL-101(Cr), molecular dynamics (MD) simulations under the same conditions as experiments are performed, and particular emphasis is given on localizing the position of the water molecules and identifying the main vibrations that contribute to the dominant peaks obtained in the spectra. The combination of the experimental DRIFTS spectroscopy with the theoretical MD simulation enables a better understanding of water molecule dynamics in the MIL-101(Cr) and functional MIL-101(Cr) cages.

Water molecules confined in the MIL-101(Cr) and two functional MIL-101(Cr) exhibit unique phases and dynamic behaviors at various sorption-desorption stages. For

the original MIL-101(Cr), in the adsorption process, the water molecules first coordinate with metal sites and form 1-D water chains from the unsaturated Cr^{3+} . As the water amount increases, the 1-D water chains grow in length and connect together, gradually forming a water monolayer on the inner surfaces of the cages. This monolayer changes the property of the surface from hydrophobic to hydrophilic, which induces the beginning of water condensation in the medium and large cages. The entire pores are filled with condensed water in the end. In the desorption process, a reverse process is observed with hysteresis. The condensed water is first desorbed from the structures, followed by the water monolayer, and finally the 1-D water chains as well as single water molecule bonded to the Cr^{3+} site are desorbed from the MIL-101(Cr).

Acknowledgements

I would like to take this opportunity to give my sincerest thanks to all those who have supported me through my Ph.D. studies.

First and foremost, I would like to thank and express my heartfelt gratitude towards my supervisor, Professor Jean-Jacques Delaunay, for guiding me in my academic career. Professor Delaunay is a serious and responsible advisor. When I started my first study in the lab, no matter how busy he was, he always accompanied me to do the experiments. He taught me how to do spectral measurement and regulated my dangerous behaviors in the laboratory. He helped me solve the most crucial problem of stress control in my research and suggested connecting two measurement instruments to obtain better results. Without him, I would not graduate so smoothly. Professor Delaunay is always curious about new things in the researches. He always encourages me to think from another direction and gives me the confidence to find out the mechanism behind these interesting phenomena. I really learned a lot from him and I want to be a researcher like him in the future.

I am deeply grateful to Professor Hirofumi Daiguji, Professor Ryotaro Matsuda, Professor Takashi Uemura, and Assistant Professor Takashi Kitao. Without their support and guidance, my Ph.D. studies could never have been possible. I would like to thank Professor Daiguji for his experimental instruments, valuable discussion, and constructive suggestions on my research, Professor Matsuda for his experimental materials and nice collaboration, and Professor Uemura and Kitao for their detailed explanation of the

preparation processes. I would also like to thank the jury in my Ph.D. defense, Professor Hitoshi Tabata, Professor Takashi Yatsui, and Professor Junho Choi. Their suggestions are of great value to my research and make me have a clearer plan for my future study. I have the privilege to have them as interactive teachers and dedicated jury members.

I would like to gratefully acknowledge Assistant Professor Ya-Lun Ho, who acted very much as a secondary supervisor to me throughout my studies, and whose invaluable knowledge helped me solve many key problems in the experiments. In daily life, Professor Ho also always encourages me and we always exchange ideas which really help me a lot. I would also like to acknowledge Mr. Shubo Fei, who has been an excellent academic colleague always eager to hear my ideas and discuss difficulties in the research with me. He helped me to do the simulation, and without him, I don't think I would have been able to graduate on time.

I would like to appreciate the members in Delaunay lab, Dr. Yi-Hsin Tai, Dr. Zhiyu Wang, Dr. Kenji Clark, Mr. Chih-zong Deng, Mr. Syazwan Kamal, Mr. Xing Di, Mrs. Chufan Zhou, Mr. Young-Jae Park, and Mr. Dairoku Meada. Thanks for their patient guidance and significant collaboration on my research as well as thanks for their kind encouragement and great support in my life. We had a wonderful time together, and I will always remember it in my heart.

I would also like to thank the CSC scholarship for the financial support which allows me to concentrate on my study without worrying too much about living. Also, I would like to thank all of the staff members in the Mechanical office and IME program office for their professional administration work.

Finally, I would like to give a special thanks to my fiancé Hanyu Liu. He provides me with a place where I can share my joy and sorrow without any worries, and I know that no matter what happens, he will always stand behind me and support me. I would also like to express my deepest gratitude to my parents, who always support me, trusted me, and give me the courage to keep on fighting.

Table of Contents

Abstract	i
Acknowledgements	vi
List of Figures	xii
List of Tables	xiv
Chapter 1: Introduction	1
1.1 Future of Cooling	1
1.2 Air conditioning units	2
1.2.1 Compression-evaporation cycle based AC units	2
1.2.2 Sorption-desorption cycle based AC units	4
1.3 Conventional porous materials for sorption-desorption cycle	6
1.3.1 Zeolites	6
1.3.2 Silica gel	7
1.4 Superior porous materials for sorption-desorption cycle	8
1.4.1 Development of MOFs	9
1.4.2 Applications of MOFs	11
1.4.3 MIL-101(Cr)	13
1.5 Research goal and thesis structure	16
1.5.1 Research goal	16
1.5.2 Thesis structure	17
Chapter 2: Synthesis and characterization of MIL-101(Cr).....	19

2.1 MIL-101(Cr) Synthesis	19
2.1.1 Materials and instruments for MIL-101(Cr) synthesis	19
2.1.2 Procedures for MIL-101(Cr) synthesis	20
2.1.3 Functionalization of MIL-101(Cr)	22
2.2 MIL-101(Cr) Characterization	23
2.2.1 Description of material structures	24
2.2.2 SEM for surface morphology	25
2.2.3 XRD for crystal information	27
2.2.4 Raman spectroscopy for structural information	28
2.2.5 Nitrogen sorption-desorption for pores properties	29
2.2.6 Water sorption-desorption for isotherm	31
Chapter 3: Diffuse reflectance infrared spectroscopy and molecular dynamics simulation	34
3.1 Diffuse reflectance infrared spectroscopy (DRIFTS)	34
3.1.1 Working principle of DRIFTS	35
3.1.2 Y-axis: Kubelka-Munk value	36
3.3 Molecular dynamics simulation	37
3.3.1 Force-field parameters	38
3.3.2 Water molecule models	40
3.3.3 Numerical set-up	41
3.3.4 Structural properties	42

3.3.5 Dynamic properties.....	43
Chapter 4: Water adsorption and desorption behaviors in MIL-101(Cr) and functional MIL-101(Cr)	44
4.1 Effect of cages properties of MIL-101(Cr) on water sorption-desorption behaviors.....	44
4.1.1 Water phases and dynamic behaviors in MD simulation	44
4.1.2 Water phases in DRIFTS spectra	47
4.1.3 Water dynamic behaviors in DRIFTS spectra.....	55
Chapter 6: Conclusions and future Work	60
References	62

List of Figures

Figure 1-1 (a) Share of global electricity demand for housing growth to 2050. (b) Percentage of households equipped with AC in selected countries in 2018.	2
Figure 1-2 Principle of a compression-evaporation cycle based AC unit.	3
Figure 1-3 Principle of a sorption-desorption cycle based AC unit.	5
Figure 1-4 Water adsorption and desorption isotherms on different zeolites: DF-9, DF-9 (after microwave irradiation), 4A, and OXYSIV-5 at 30°C.	7
Figure 1-5 Water adsorption and desorption isotherm on silica gel at 50°C.....	8
Figure 1-6 Illustration of crystal structures of different metal-organic frameworks.....	9
Figure 1-7 Different applications of metal-organic frameworks.....	12
Figure 1-8 Variation of water adsorption amount of the MIL-101(Cr) and some other MOFs in ten sorption-desorption cycles.....	15
Figure 2-1 (a) Glass vacuum filtration unit and (b) water bath with magnetic stirring parts used in the synthesis. (c) Synthesized MIL-101(Cr) sample powder.....	20
Figure 2-2 Illustration of synthesis procedures for the MIL-101(Cr).	21
Figure 2-3 Structures of (a) MIL-101(Cr)-SO ₃ H and (b) MIL-101(Cr)-NO ₂	23
Figure 2-4 Illustration of the 3D crystal structures of the MIL-101(Cr).	25
Figure 2-5 Different magnifications of SEM images of synthesized MIL-101(Cr): (a) ×10k and (b) ×70k.	26
Figure 2-6 Experiment measured and simulated XRD patterns of synthesized MIL-101(Cr).	28
Figure 2-7 Experiment measured Raman spectrum of synthesized MIL-101(Cr).	29
Figure 2-8 Nitrogen sorption-desorption isotherm of synthesized MIL-101(Cr) at -196°C. Inset: pore size distribution obtained by the NLDFT method.	31
Figure 2-9 Water sorption-desorption isotherm of synthesized MIL-101(Cr) at 25°C..	33

Figure 3-1 Working principle of diffuse reflectance infrared spectroscopy.	36
Figure 4-1 Phases and dynamic behaviors of water molecules in the 34 Å and 29 Å cages, and 8 Å super-tetrahedron of the MIL-101(Cr) simulated by MD simulation.....	47
Figure 4-2 Different water sorption sites in MD simulation when only a small amount of water molecules is loaded.....	47
Figure 4-3 Variation of DRIFTS spectra of the MIL-101(Cr) at different air pressures in (a) adsorption and (b) desorption processes.	50
Figure 4-4 (a) DRIFTS spectrum of $\text{H}_2\text{O}\cdots\text{Cr}$ and $(\text{H}_2\text{O})_n\cdots\text{H}_2\text{O}\cdots\text{Cr}$ in the MIL-101(Cr) at 6 Pa. (b) MD simulated vibration frequency spectra for different water molecules. .	51
Figure 4-5 MD simulated vibration frequency spectra of water molecules (in red with underline) in the 1-D water chains.	52
Figure 4-6 Variation of DRIFTS spectra of the liquid-like water in the MIL-101(Cr) with the increased air pressures.	54
Figure 4-7 (a) DRIFTS spectrum of liquid-like water in the MIL-101(Cr) at 1 atm. (b) Infrared spectrum of bulk water at 25°C with three Gaussian components.....	54
Figure 4-8 Deconvolution of the DRIFTS spectra with six Gaussian components for the air pressures, and area variation of them in the sorption-desorption processes.	59
Figure 4-9 Hysteresis between the adsorption and desorption processes of six Gaussian components (from G1 to G6).	59

List of Tables

Table 1-1 Metal coordination sites, organic ligands, and formed structures of different series of MOFs.	11
Table 1-2 Comparison of water uptake capacities of the MIL-101(Cr) and some other MOFs.	14
Table 3-5 L-J potential function parameters and charges of the atoms used in MD simulation.	40
Table 3-6 Coefficients used in flexible SPC/E model in MD simulation.	41
Table 4-1 Characteristic DRIFTS peaks of different types of water in the MIL-101(Cr).	55

Chapter 1: Introduction

1.1 Future of Cooling

Cooling devices, such as air conditioning (AC) units, have become one of the most energy-consuming aspects of our modern life [1]. According to the International Energy Agency, the use of air conditioners and electric fans to stay cool currently accounts for more than 10% of the total electricity used in housing around the world [2]. When we go to 2050, as shown in Figure 1-1a, the energy demand for space cooling will increase to around 37%, which is almost three times than today. Moreover, around 2/3 of the world's households will have an air conditioner by 2050. Compared with the percentage of the households equipped with AC in the selected countries as shown in Figure 1-1b, the number of AC units is also expected to triple over the next 30 years, particularly due to the increased income in developing countries, many of which are located in tropical or subtropical regions of the world [3–5].

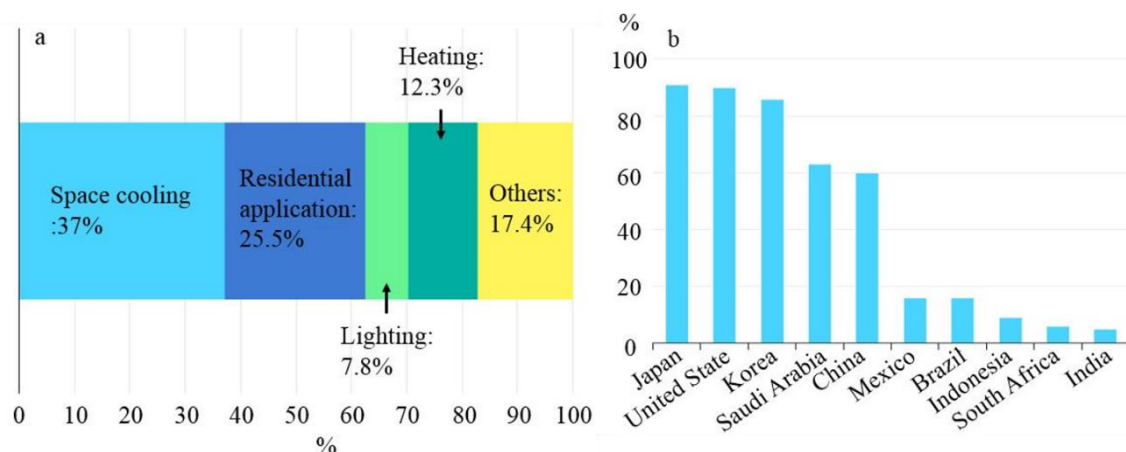


Figure 1-1 (a) Share of global electricity demand for housing growth to 2050. (b) Percentage of households equipped with AC in selected countries in 2018 [6]. Source: IEA (2018) The Future of Cooling, <https://www.iea.org/reports/the-future-of-cooling>, All rights reserved.

The increased use of conventional AC units will be harmful to the environment, as it is not good for CO₂ reduction [7]. That is because that the operation of air conditioning needs electricity, and a large amount of CO₂ will be produced during the electricity generation processes. According to the International Energy Agency, fossil fuel power generation is still the primary method for electricity generation, accounting for 65% of the global total electricity generation amount. For every kilowatt-hour of electricity produced, an average of 505 grams of CO₂ will be emitted into the atmosphere, which becomes the leading cause of global warming today. Therefore, in the face of the dramatic increase of AC units, to reduce CO₂ emission and prevent the atmospheric environment from deteriorating, the efficiency of AC units needs to be improved. Moreover, if clean energy, e.g., solar energy, geothermal energy, and industrial waste heat, can be used to drive refrigeration, not only the total operating costs will be significantly reduced, but also environmentally friendly development can be achieved.

1.2 Air conditioning units

1.2.1 Compression-evaporation cycle based AC units

Compression-evaporation cycle based AC units have been proposed for over a century and become the most commonly used method for cooling in our daily life today [8]. This conventional AC unit always consists of four main parts: a compressor, a

throttling device (capillary or expansion valve), a condenser, and an evaporator. The working principle of it is shown in Figure 1-2. During the refrigeration process, the compressor first compresses the gaseous refrigerant into the high temperature and pressure state by using electric energy. The compressed gaseous refrigerant then enters the condenser and liquefies into the liquid with giving off the heat. The liquid refrigerant goes through the throttling device to decrease the pressure, and then it enters the evaporator. In the evaporator, the liquid refrigerant absorbs heat and evaporates into the gaseous state again so that desired cold is produced. This gaseous refrigerant finally goes back to the compressor, and then a new refrigeration cycle can be started.

One problem of conventional compression-evaporation cycle based AC units is that the flammable and toxic hydrogenated chlorofluorocarbons are always used as the working refrigerants [2], e.g., R-11, R-12, and R-22 HCFC. Compared to CO₂, these kinds of refrigerants will produce a more severe impact on the atmospheric ozone layer and significantly aggravate the greenhouse effect. Therefore they are facing a fade-out process by international regulations.

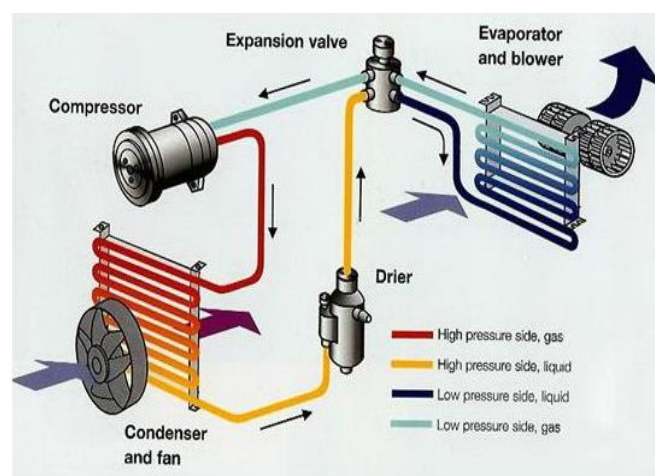


Figure 1-2 Principle of a compression-evaporation cycle based AC unit [9].

1.2.2 Sorption-desorption cycle based AC units

To address the hazardous problems and reduce the energy consumption for conventional AC units, new energy-efficient and green approaches for cooling must be developed. Recently, due to the potential of high refrigeration efficiency and energy efficient property, the sorption-desorption cycle is being considered as the cutting-edge replacement for the compression-evaporation cycle used in the air-conditioning systems [10]. In the sorption-desorption cycle, evaporation of the refrigerant is induced by the adsorption of porous adsorbents materials, and this endothermic process is used to achieve refrigeration in the end. The principle of the sorption-based AC units is shown in Figure 1-3, and the working process can be divided into four steps: at the first step from a to b, the refrigerant is evaporated from the reservoir as it is gradually adsorbed by the porous adsorbent material, and therefore at this working step, useful cold is produced, which exactly can be used to achieve the desired cooling effect. At the second step from b to c, it is an isosteric heating step, and the pressure of the refrigerant will be increased to the condenser pressure level so that the next generation step will take place. At the generation step from c to d, a driving heat from a high-temperature heat source is used to desorb the refrigerant from the adsorbent material, and then the vapor of this refrigerant is condensed in the reservoir again. This is the only step that consumes the external thermal energy in this cycle. At the last step from d to a, it is an isosteric cooling step, and the pressure of the refrigerant will be decreased to the evaporator pressure level. The refrigeration cycle for the sorption-based AC unit is finally closed.

Noticeably, for the sorption-desorption cycle based AC units, the properties of porous materials and the interaction with adsorbed refrigerant are the crucial factors to the system

performance and energy consumption, thus becoming the focus of studies and have been widely discussed [11–13]. Recently, in the sorption-desorption cycle, the commonly used adsorbents materials are porous carbon or oxygen compounds, such as zeolites and silica gel. The main working refrigerant used is water, which is harmless and has high evaporation latent [14]. Sorption-desorption cycle based AC units have always been considered as cutting-edge devices due to the development of new efficient materials that use low driving temperatures and maintain high cooling output while employing only water as the working fluid, which can enhance the cooling efficiency and reduce the energy consumption significantly.

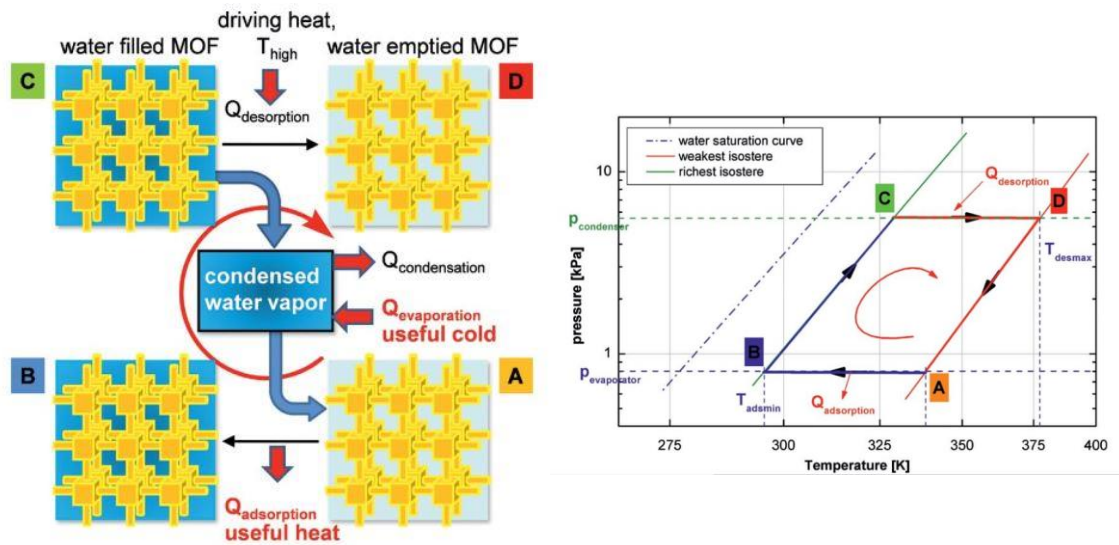


Figure 1-3 Principle of a sorption-desorption cycle based AC unit [15]. Reprinted with permission, Copyright © 2010 WILEY-VCH Verlag GmbH & Co. KGaA, Weinheim.

1.3 Conventional porous materials for sorption-desorption cycle

1.3.1 Zeolites

Zeolites [16] are a group of hydrous silicate minerals with alkali or alkaline-earth metals, which have unique porous structures and chemical properties that have been commonly used in the sorption-desorption cycle based AC units. Within the zeolites, there are many uniform pores, whose volume can account for more than 50% of the total crystal volume. Zeolite water naturally exists in these pores, and it can be adsorbed from the structures by heating the material. The specific surface area of zeolites after dehydration can increase to around 1100 m²/g [17]. For zeolites, a strong electrostatic force field and polarity are always formed within the pores structures, enhancing the adsorption for water molecules in the air, so that it can still maintain a certain amount of water within the structures at lower humidity and higher temperature condition [18]. However, this strong interaction between the pores and water molecules leads to a high driving temperature (>150°C) that is needed to be applied when water is desorbed from the material [7]. The high driving temperature means more energy will be consumed in the refrigeration process by using zeolite as the adsorbent, and with this high driving temperature, the desired low-grade energy sources cannot be used. Therefore, to enhance the water adsorption performance and reduce the energy required for the desorption, activation and acidic treatments are always performed, as well as some other materials are used to form the compounds with zeolites in the current researches [19–21].

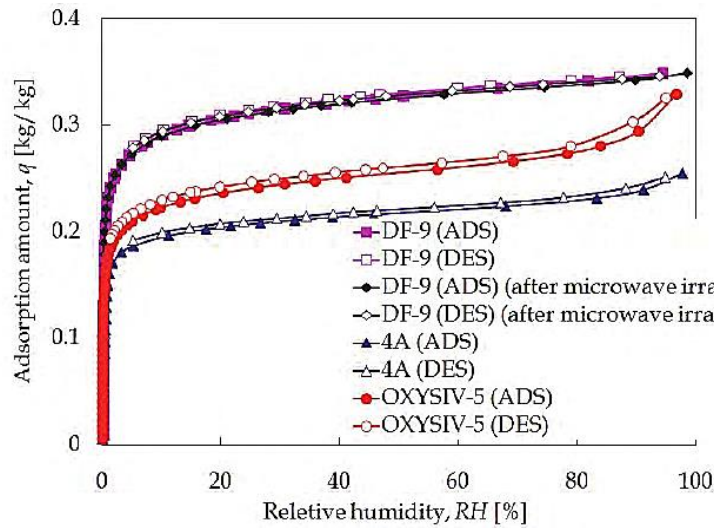


Figure 1-4 Water adsorption and desorption isotherms on different zeolites: DF-9, DF-9 (after microwave irradiation), 4A, and OXYSIV-5 at 30°C [22].

1.3.2 Silica gel

Silica gel [23] is another commercial porous material that has been commonly used in sorption-desorption cycle based AC units. It is a highly active amorphous porous material, which is composed of many spherical particles with different sizes from 2 to 20 nm. The formula of silica gel is $\text{SiO}_2 \cdot n\text{H}_2\text{O}$, meaning that it has an incompletely dehydrated polymeric structure of colloidal silicic acid. As an adsorbent, because of the cross-chain structures of siloxane ($-\text{Si}-\text{O}-\text{Si}-$) and the existence of many silanol groups (SiOH) on the surface, water molecules are easily adsorbed by the dispersion and polar forces to form the hydrogen bonded water network within the structures of silica gel [24]. Moreover, silica gel has a relatively high surface area, which is around $450 \text{ m}^2/\text{g}$, so that it processes a high water uptake capacity, and the water molecules on the surface can be easily desorbed when silica gel is heated to about 90°C . The silanol group can maintain its properties up to 500°C , meaning that silica gel also has high thermal stability. However,

although silica gel has relatively strong adsorption to the water molecules, the water uptake capacity of zeolite is 2-5 times higher than that of it [25]. And with the increase of water amount, the water adsorption capacity of silica gel decreases obviously as it is related to the residual amount of the silanol groups on the surface. Therefore, to enhance the water adsorption performance, silica gel is always modified and mixed with other different sizes of silica gel in the current researches [26–28].

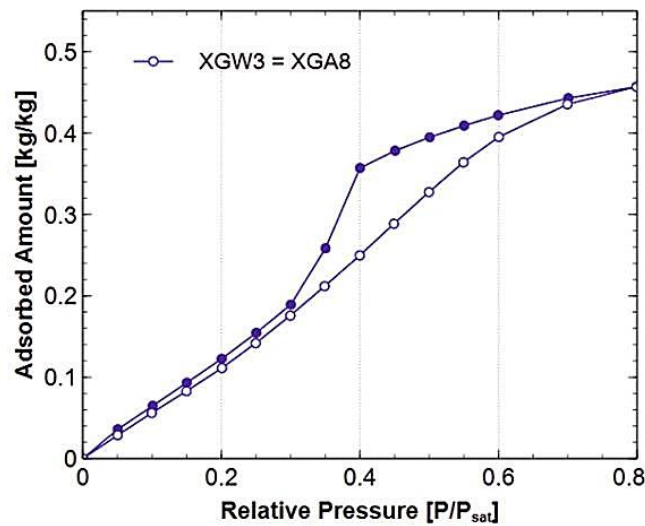


Figure 1-5 Water adsorption and desorption isotherm on silica gel at 50°C [29].

1.4 Superior porous materials for sorption-desorption cycle

Metal-organic frameworks (MOFs) are a group of porous materials that with periodic network structures formed by self-assemble action of metal coordination sites and organic ligands under certain different conditions, as shown in Figure 1-6. As a new type of organic-inorganic composites functional materials, MOFs not only have three-dimensional pore structures like inorganic porous materials but also have flexible composition adjustability like organic materials. The high specific surface area and

porosity, as well as the designable and adjustable porous structures make MOFs become the focus of the current researches [30–34].

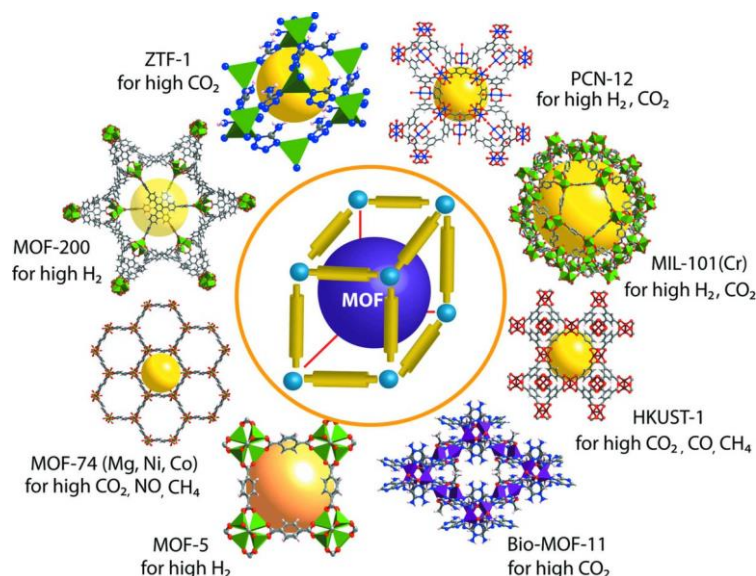


Figure 1-6 Illustration of crystal structures of different metal-organic frameworks [35].

Reprinted with permission, Copyright © 2013 International Union of Crystallography.

1.4.1 Development of MOFs

In 1995, Yaghi et al. prepared a new porous material with two-dimensional structures ($\text{CoC}_6\text{H}_3(\text{COOH}_{1/3})_3(\text{NC}_5\text{H}_5)_2 \cdot 2/3\text{NC}_5\text{H}_5$) by using the trimesic acid as well as transition metal cobalt and proposed the new concept of metal organic frameworks for the first time [36]. In 1999, Yaghi et al. used terephthalic acid as the organic ligand and zinc as the metal site to synthesize a new porous material labeled as MOF-5, and this material has been widely concerned because of its ultra-high surface area [37]. In 2002, based on MOF-5, Yaghi et al. synthesized a series of materials with three-dimensional network structures labeled as IRMOFs series by adjusting the types of the organic ligands [38]. In 2006, Yaghi et al. used imidazole as the organic ligand and zinc as well as cobalt as metal

sites to synthesize a series of molecular sieve-like imidazole framework materials labeled as ZIFs series [39]. In the next few decades, with the development of coordination chemistry, metal organic frameworks with various structures were proposed, and according to the statistics of the Cambridge crystal database, more than one hundred thousand MOFs have been recorded up to now. Among these MOFs, there are several common series: isorecticular metal-organic framework (IRMOFs) series [38], zeolitic imidazolate framework (ZIFs) series [39], materials of Institut Lavoisier (MIL) series [40], coordination pillared-layer (CPL) series [41], porous coordination network (PCN) series [42], and University of Oslo (UiO) series [43]. The metal coordination sites, organic ligands, and formed structures of these different series of MOFs are shown in Table 1-1.

Table 1-1 Metal coordination sites, organic ligands, and formed structures of different series of MOFs.

MOFs	Metal sites	Organic ligands	Structures
IRMOFs	Zn_4O^{6+}	aromatic carboxylic ligands	octahedral
ZIFs	Zn^{2+} , Co^{2+}	imidazole ligands	tetrahedral
CPL	tetravalent metallic element	pyrazine carboxylic ligands	pillared
MIL	Cr^{3+} , Al^{3+} , Fe^{3+}	terephthalic acid ligands, pyromellitic acid ligands	octahedral
PCN	Cu^{2+}	anthracene derivative ligand	octahedral
UiO	Zr^{4+}	terephthalic acid ligands	octahedral, tetrahedral

1.4.2 Applications of MOFs

Due to their peculiar coordination structures, controllable organic ligands, tailor-made porous morphologies, and large Langmuir surface areas, metal-organic frameworks have become widely studied as candidates for separation processes [44], catalytic processes [45], and gas storage [46] (see Figure 1-7). Guo et al. synthesized three new water-stable In(III)-based metal organic frameworks with rod-shaped secondary building units and proved that all of them have an excellent performance on selectively adsorbing C_2H_2 over CO_2 and CH_4 [47]. Juan-Alcañiz et al. investigated two metal organic frameworks bearing sulfonic acid moieties, and the results showed that when using Zr as the metal node, the structure exhibited the highest activity and full re-usability in the

esterification of n-butanol with acetic acid [48]. With hydrogen dissociation and spillover, Li et al. enhanced the hydrogen uptakes of MOF-5 and IRMOF-8 by a factor of 3.3 and 3.1 to realize hydrogen storage at ambient temperature [49]. All these researches have proved that metal-organic frameworks have great prospects in these applications.

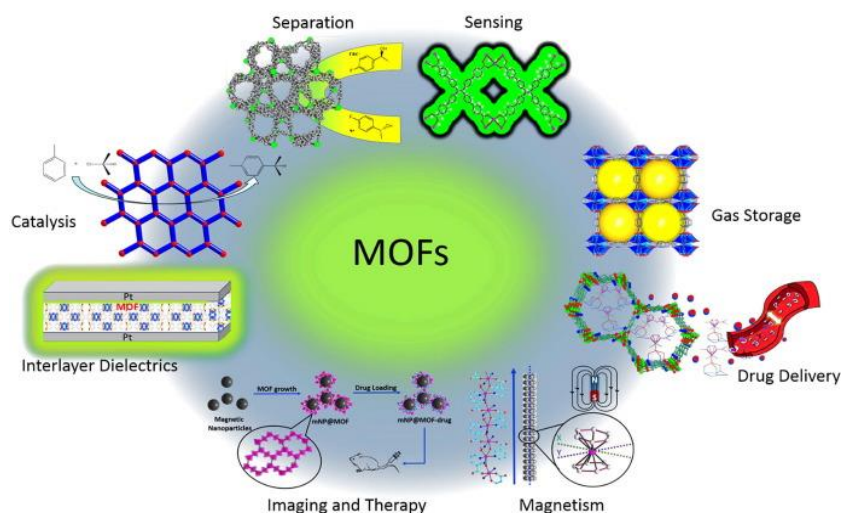


Figure 1-7 Different applications of metal-organic frameworks [50]. Reprinted with permission, Copyright © 2018 Elsevier B.V. All rights reserved.

In addition to the above mentioned applications, as for the porous material, metal-organic frameworks also have great advantages in the water sorption-desorption aspect. Wade et al. described the modular synthesis of Zn (NDI-X), featuring infinite chains of tetrahedral Zn^{2+} ions bridged by pyrazolate groups as well as around 16 Å-wide channels with functionalized naphthalenediimide linkers, and studied their water uptake capacities [51]. Ghosh et al. simulated adsorption isotherms for water in UiO-66 and illustrated the role of the structural defects in its water adsorption capacities [52]. Han et al. presented molecular simulation as well as experimental investigation for water adsorption on aluminum fumarate (Al-fum) MOFs, and the results showed that a faster kinetic with a

higher water transfer could be achieved by combining the CHA-zeolite and Al-fum-MOF [53]. There are still many other researches on the water sorption-desorption capacities of different types of MOFs. Among all these researches, a unique MOF labeled as MIL-101(Cr) is the most attractive material that cannot be ignored as it has a great potential to become an ideal porous material used in the sorption-desorption cycle.

1.4.3 MIL-101(Cr)

MIL-101(Cr) is one of the most representative materials in metal-organic frameworks, and it is first proposed by Férey et al. in 2006 [40]. MIL-101(Cr) is a chromium terephthalate-based solid, and it is unique in terms of the hierarchical cages with large diameters of 29 Å and 34 Å (window aperture of 12 Å and 16 Å), as well as the corresponding huge pore volume of 12,700 Å³ and 20,600 Å³ [40]. Moreover, MIL-101(Cr) possesses high hydrothermal stability that can retain structural integrity up to 240°C [14], which is higher than other similar porous materials, implying that this material is suitable for hydrothermal applications. Table 1-2 shows the comparison of water uptake capacities of the MIL-101(Cr) and some other MOFs. Noticeably, MIL-101(Cr) has the largest surface area of 2579 m²/g and pore volume of 1.63 cm³/g. It also processes the highest water uptake of 1263 g/kg, and 98% of water can be desorbed from this material during the desorption process. Figure 1-8 shows the variation of water adsorption amount of the MIL-101(Cr) and some other MOFs in ten sorption-desorption cycles. Compared to other MOFs, there is almost no decrease of the water adsorption amount of the MIL-101(Cr) after ten cycles, indicating that it indeed has high hydrothermal stability that is suitable to be used the sorption-desorption cycle based AC units.

Table 1-2 Comparison of water uptake capacities of the MIL-101(Cr) and some other MOFs [12].

MOFs	SA (m ² /g ⁻¹)	V _p (cm ³ /g ⁻¹)	Uptake capacity (g/kg ⁻¹)	Working capacity (g/kg ⁻¹)	Water desorbed (%)
Ti-MIL-125	1153	0.47	323	313	97
Ti-MIL-125-NH ₂	1358	0.55	413	409	99
Zr-UiO-66	959	0.40	347	338	97
Zr-UiO-66-NH ₂	1109	0.46	364	355	998
Zr-MOF-808	1880	0.69	744	714	96
Cr-MIL-101	2579	1.63	1263	1246	98
Cu-HKUST-1	1512	0.41	218	105	48
Al-MIL-53	814	0.41	13	2	15
Zn-ZIF-8	1835	0.69	15	6	40

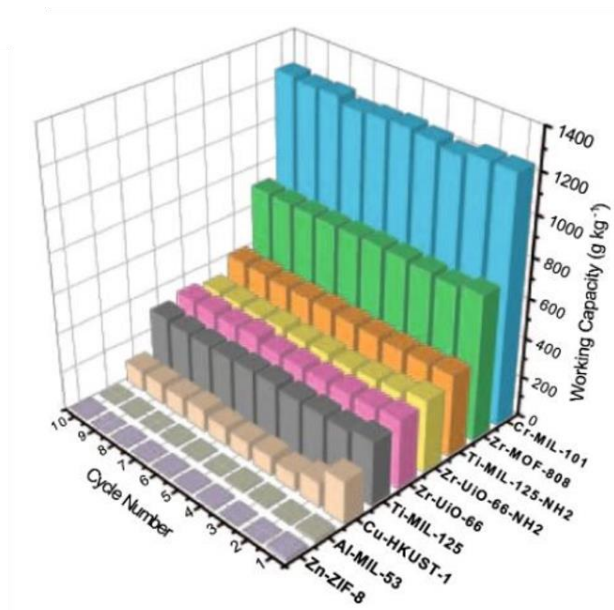


Figure 1-8 Variation of water adsorption amount of the MIL-101(Cr) and some other MOFs in ten sorption-desorption cycles [12].

Due to these excellent physical properties and great potential to become an ideal porous material used in the sorption-desorption cycle, the uptake capacity of water adsorbed in the MIL-101(Cr) has been studied. Permyakova et al. used the MIL-101(Cr) as a host matrix of salts for the preparation of a composite water sorbent and analyzed the effect of its physico-chemical as well as structural properties on the water sorption performance [54]. Khutia et al. synthesized different types of functional MIL-101(Cr) and found that the $-pNH_2$ group showed the largest water uptake as well as the highest hydrothermal stability [55]. Yan et al. prepared a novel composite with MIL-101(Cr) and graphene oxide and proved that this material possessed a super-high adsorption capacity for water [56].

Among these current studies, it is not difficult to find that researchers mainly focus on how to enhance the water adsorption property of MIL-101(Cr) and how to reduce the energy requirement in the desorption process by adding various functional groups, optimizing the pore structures, and adjusting the component elements. Although directly improving the performance is essential, the research of the water sorption-desorption mechanism of MIL-101(Cr), especially the dynamic phase transitions of water molecules confined in the cages, is also an indispensable part that needs to be comprehensively analyzed not only for its real industrial applications but also for the further development of superior materials used in the sorption-desorption cycle based AC units.

1.5 Research goal and thesis structure

1.5.1 Research goal

Sorption-desorption cycle of water used in air conditioning systems is proposed as the most potential method to satisfy the increasing energy demand for space cooling in the next few decades. As the critical issue to enhance the cooling efficiency and reduce energy consumption, MIL-101(Cr), processing unique cages structures and superior physical properties, is considered as the most suitable porous absorbent that can be used in the sorption-desorption cycle. Although the thermal performance of sorption-based AC units can be estimated using the amount of water loaded on the MIL-101(Cr) as determined from water sorption-desorption isotherm, the behavior of this porous material, especially the phases of water incorporated in the matrix of the MIL-101(Cr) (confinement effect) and the stability of the MIL-101(Cr) (break down by hydrolysis)

upon sorption-desorption cycling, is still not fully elucidated so that the design of high efficient sorption-desorption cycle based AC units is still hampered now.

In this regard, we propose to perform the infrared vibrational mode analysis of the MIL-101(Cr) and two functional MIL-101(Cr) together with incorporated water during the sorption-desorption cycle. The goal of this fundamental research is to analyze the phases and dynamic behaviors of water molecules that confined in cages structures of the MIL-101(Cr), MIL-101(Cr)-SO₃H, and MIL-101(Cr)-NO₂ to help the further development of superior materials of high-efficiency sorption-desorption cycle based AC units.

1.5.2 Thesis structure

The following thesis provides an in-depth study of the water phases and dynamic behaviors in the MIL-101(Cr) and two functional MIL-101(Cr). Chapter 1 provides a brief background of research on the necessity of using sorption-based AC units and the conventional as well as the new efficient porous materials that have been proposed for this application. In chapter 2, the synthesis materials and procedures of the MIL-101(Cr) and two functional MIL-101(Cr) are proposed. Meanwhile, the characterization, including the scanning electron microscopy, X-ray diffraction, Raman spectrum, as well as nitrogen and water adsorption isotherms of the MIL-101(Cr) are discussed. Chapter 3 outlines the analysis methods used in this study: Diffuse reflectance infrared spectroscopy (DRIFTS) and molecular dynamics (MD) simulation. For DRIFTS, the principle of it and the corresponding Y-axis, Kubelka-Munk value, are studied. The preparation of the DRIFT spectrometer is described, and the measurement procedures are summarized. For

MD simulation, the force-field parameters and the water molecule models are proposed. The calculation of the radial distribution function, order parameter, and average hydrogen bond number are discussed. Chapter 4 and chapter 5 are results and discussion parts. In chapter 4, the effect of cages properties of the MIL-101(Cr) on water phases and dynamic behaviors are comprehensively studied. Finally, in chapter 6, the key conclusions of this study are detailed, and the future avenues of potential researches are summarized.

Chapter 2: Synthesis and characterization of MIL-101(Cr)

2.1 MIL-101(Cr) Synthesis

2.1.1 Materials and instruments for MIL-101(Cr) synthesis

Main materials that used in the MIL-101(Cr) synthesis are 1,4-benzenedicarboxylic acid (H_2BDC , 99% purity), chromium(III) nitrate ($\text{Cr}(\text{NO}_3)_3 \cdot 9\text{H}_2\text{O}$, 99% purity), hydrofluoric acid (HF , 99% purity), ethanol (EtOH , 99% purity), dimethylformamide (DMF , 99% purity), ammonium fluoride (NH_4F , 99% purity) and deionized water (H_2O , HPLC grade).

Main instruments and apparatus used in the MIL-101(Cr) synthesis (see Figure 2-1) are electric oven, vacuum chamber, glass vacuum filtration unit, water bath with magnetic stirring parts, Teflon-lined stainless steel autoclave vessel, hydrothermal container, polytetrafluoroethylene membrane (PTFE, $0.2\ \mu\text{m}$), grid ($100\ \mu\text{m}$), analytical balance, pipette, and gloves.

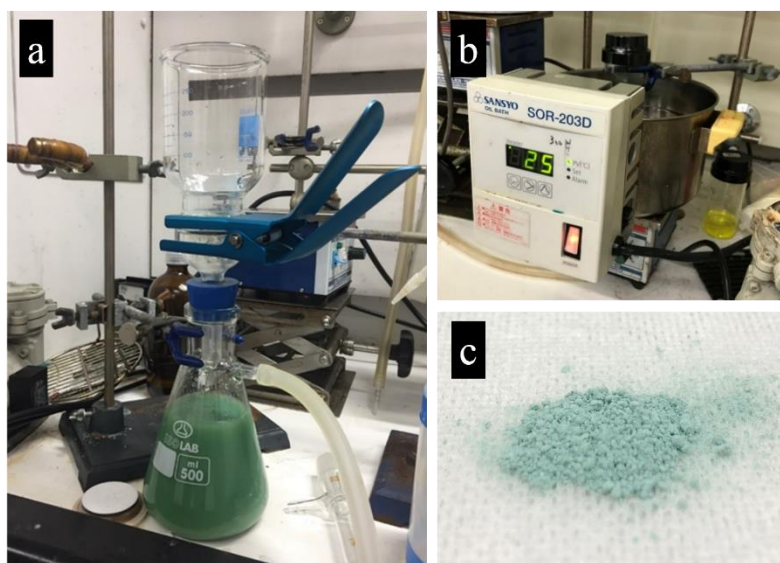


Figure 2-1 (a) Glass vacuum filtration unit and (b) water bath with magnetic stirring parts used in the synthesis. (c) Synthesized MIL-101(Cr) sample powder.

2.1.2 Procedures for MIL-101(Cr) synthesis

MIL-101(Cr) is prepared using a scaled-up version of the reported hydrothermal reaction [57–59]. The main procedures are shown as follows (see Figure 2-2):

2.1.2.1 For synthesis

- (1) Terephthalic acid (8.0 mmol) and $\text{Cr}(\text{NO}_3)_3 \cdot 9\text{H}_2\text{O}$ (8.0 mmol) are first mixed with the aqueous HF (48wt% solution in water, 8.0 mmol HF) and deionized water (50 ml) in a 100 ml Teflon-lined autoclave vessel.
- (2) The obtained mixed solution is then heated at 220°C for 8h by an electric oven.
- (3) Wait for the mixed solution naturally cooling down to room temperature in the end.

2.1.2.2 For purification

- (1) The mixed solution after synthesis is first filtered over a 100 μm grid to remove the unreacted terephthalic acid crystals, which will be solid that remained on the grid, with the use of the glass vacuum filtration unit.
- (2) The solution in the previous step is collected and then filtered with the 0.2 μm PTFE membrane.
- (3) The filtered green powder is collected and then washed by methane to remove the water in these powder.
- (4) The powder is then dried in a vacuum chamber.

- (5) The dried powder is mixed with EtOH and heated at 80°C for 3h with stirring by the use of the water bath.
- (6) The mixed solution is then filtered with the 0.2 µm PTFE membrane and 100 µm grid and vacuumed to dry state in a vacuum chamber.
- (7) The dried powder is mixed with DMF and heated at 100°C for 3h with stirring by the use of the water bath.
- (8) The mixed solution is then filtered with the 0.2 µm PTFE membrane and 100 µm grid and vacuumed to dry state in a vacuum chamber.
- (9) The dried powder is mixed with NH₄F and heated at 90°C for 16h with stirring by the use of the water bath.
- (10) The mixed solution is then filtered with the 0.2 µm PTFE membrane and 100 µm grid. The obtained wet powder is then copiously washed with deionized water.
- (11) The wet powder is finally heated at 150°C under vacuum overnight to degas, and the green MIL-101(Cr) powder is synthesized in the end.

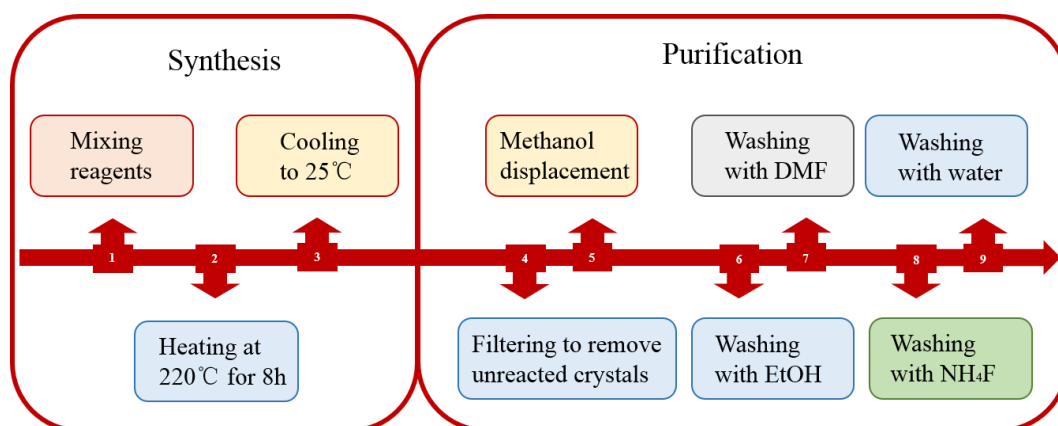


Figure 2-2 Illustration of synthesis procedures for the MIL-101(Cr).

2.1.3 Functionalization of MIL-101(Cr)

After obtaining the original MIL-101(Cr) powder sample, the functionalization process is performed to synthesis two functional MIL-101(Cr): MIL-101(Cr)-SO₃H and MIL-101(Cr)-NO₂. The schematic structures of them are shown in Figure 2-3.

2.1.3.1 For MIL-101(Cr)-SO₃H

MIL-101(Cr)-SO₃H is prepared according to the reported hydrothermal reaction [58,60]. Briefly, monosodium 2-sulfoterephthalic acid (C₈H₅NaO₇S, 3.35 g, 12.5 mmol) and chromium trioxide (CrO₃, 1.25 g, 12.5 mmol) are first dissolved in concentrated aqueous hydrochloric acid (HCl, 0.91 g, 25 mmol) and deionized water (50 mL) in a Teflon-lined stainless steel autoclave vessel. The mixed acidic solution is heated at 180°C for 6 days under the hydrothermal condition and then cool down to room temperature in the end. The mixed solution is then filtered, and the obtained powder is washed three times each with EtOH (100 mL) and deionized water (400 mL). The obtained wet powder is then dried in the air, and finally the MIL-101(Cr)-SO₃H sample powder is synthesized. The yield based on chromium was 50%. The specific experimental procedures and instruments described here are similar to those used for the MIL-101(Cr) synthesis.

2.1.3.2 For MIL-101(Cr)-NO₂

MIL-101(Cr)-NO₂ is prepared according to the reported hydrothermal reaction [61,62]. Briefly, nitroterephthalic acid (H₂BDC-NO₂, 2.64 g, 12.5 mmol) and chromium trioxide (CrO₃, 1.25 g, 12.5 mmol) are first dissolved in hydrochloric acid (HCl, 1.8 g, 50 mmol) and deionized water (50 mL) in a Teflon-lined stainless steel autoclave vessel. The mixed acidic solution is heated at 180°C for 6 days under the hydrothermal condition and then cool down to room temperature in the end. The mixed solution is then filtered, and

the obtained powder is washed three times each with EtOH (100 mL) and deionized water (400 mL). The obtained wet powder is then dried in the air, and finally the MIL-101(Cr)-NO₂ sample powder is synthesized. The yield based on chromium was 55%. The specific experimental procedures and instruments described here are similar to those used for the MIL-101(Cr) synthesis.

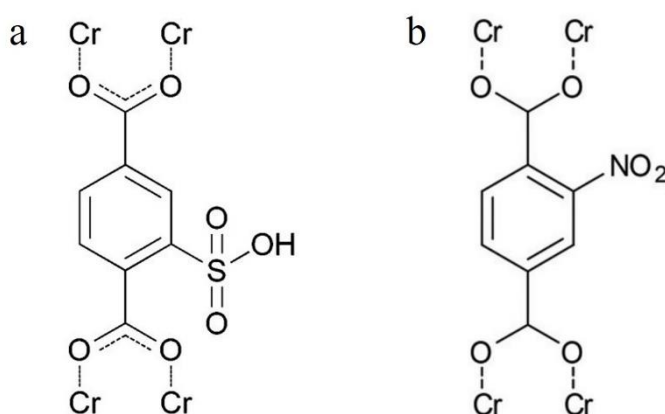


Figure 2-3 Structures of (a) MIL-101(Cr)-SO₃H [63]. (b) MIL-101(Cr)-NO₂ [64], Reprinted with permission, Copyright © 2014 Royal Society of Chemistry.

2.2 MIL-101(Cr) Characterization

MIL-101(Cr) is a unique mesoporous material. After synthesizing, the three-dimensional (3D) crystal structures, scanning electron microscopy (SEM, JEDL JSM-7000F), X-ray diffraction (XRD, SmartLab 3kW) measurement, Raman spectrum (BWTEK i-Raman pro), nitrogen adsorption, and water adsorption (MicrotracBEL Belsorp II MAX) are performed to characterize the synthesized MIL-101(Cr) sample powder.

2.2.1 Description of material structures

Figure 2-4 shows the 3D crystal structures of the MIL-101(Cr). As mentioned above [40], the metal sites of the MIL-101(Cr) is Cr, and the organic ligand is the terephthalic acid. Three Cr atoms with four oxygen atoms form a Cr trimer with an octahedral structure. In that four oxygen atoms, one is a vertex μ_3 -O atom, and one comes from the terminal groups, like water or fluorine. Four vertices Cr trimers with the organic linkers located at the six edges of them form the supertetrahedron (ST) structures in the MIL-101(Cr). The ST is a microporous cage, and the diameter of it is 8 Å. Except for these STs, there are two other mesoporous cages structures in the MIL-101(Cr). One is the medium cage delimited by 20 STs, and the internal free diameter of it is 29 Å with only the pentagonal window of 12 Å. The other is the large cage that is delimited by 28 STs, and the internal free diameter of it is 34 Å with both the pentagonal and hexagonal windows of 14.5 Å and 16 Å. The medium cages and large cages are present in a 2:1 ratio, and with these opening apertures, the guest molecules can be easily accessible to the structures of the MIL-101(Cr) during the various applications.

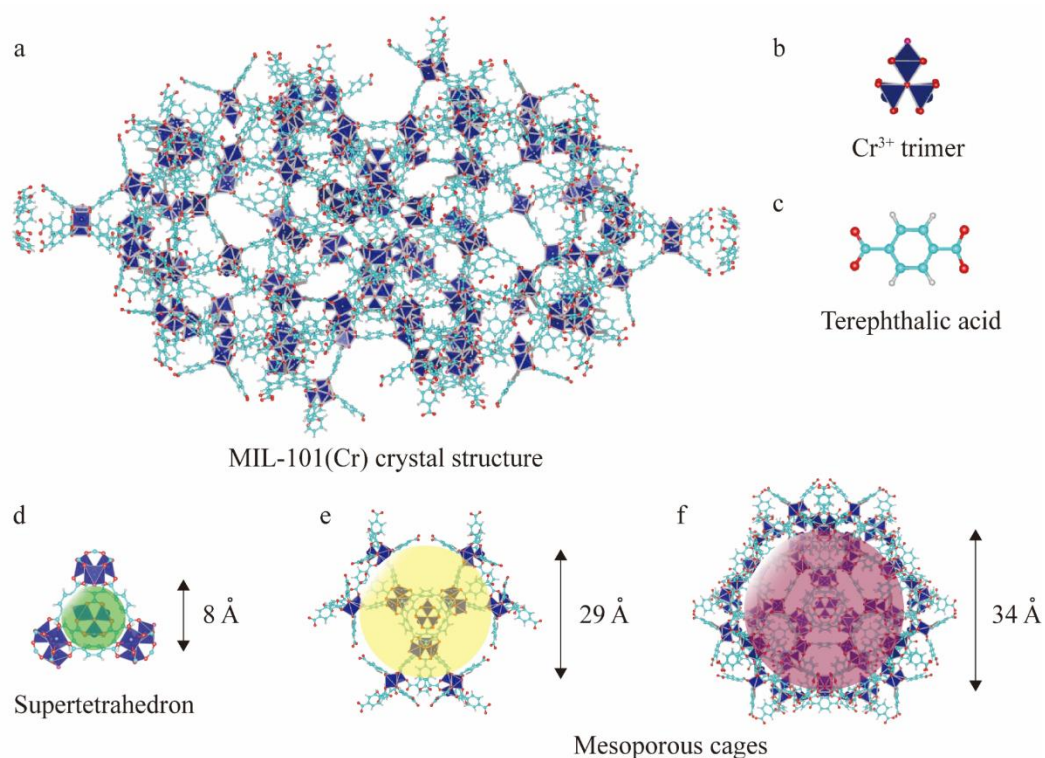


Figure 2-4 (a) Illustration of the 3D crystal structures of the MIL-101(Cr). (b) Trimer of Cr octahedra sharing a common vertex $\mu_3\text{-O}$ atom. (c) Organic ligand consisting of 1,4-benzenedicarboxylate. (d) Super-tetrahedron (8 Å) and mesoporous cages in the MIL-101(Cr): (e) medium cage (29 Å) and (f) large cage (34 Å). The Cr, C, O, H, and F atoms are in navy, blue, red, white, and pink, respectively.

2.2.2 SEM for surface morphology

Scanning electron microscopy (SEM) is a standard method to observe the microstructure of various materials. The working principle of it is like this: sample surface is first scanned by a very narrow electron beam which is emitted from a triode electron gun and forced with several accelerating electric fields. Then, the feedback electrons will form an electrical signal and be collected to the kinescope, and finally present as high-quality images, containing detailed structural information of the sample, on the display

screen. There are several advantages of this method such as simple sample preparation, adjustable magnification (between $20\text{-}20\times 10^4$ times), high image resolution, and direct observation of the sample surface structures. Therefore, SEM is applied to observe the crystal structures of synthesized MIL-101(Cr) in this study, and the electron images are shown in Figure 2-5.

Obviously, the synthesized MIL-101(Cr) is a solid material that has a regular octahedral structure with smooth surfaces and intact crystals. The average length of its edge is 874 nm, and the particle size is relatively uniform. There are no rod-like crystalline structures that can be observed, which may result from the recrystallization of the terephthalic acid, proving that the synthesis is successful and the purification of the MIL-101(Cr) is sufficient.

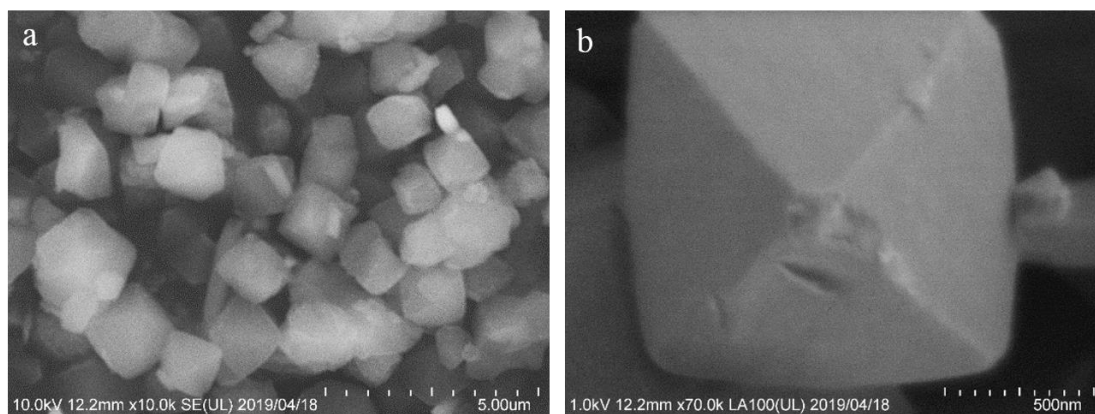


Figure 2-5 Different magnifications of SEM images of synthesized MIL-101(Cr): (a) $\times 10\text{k}$ and (b) $\times 70\text{k}$.

2.2.3 XRD for crystal information

X-ray diffraction (XRD) is a convenient method to study the internal crystal information of various materials. By analyzing the X-ray diffraction, the constituent elements, crystal structures, crystal size, and crystallinity of the sample can be easily determined so that this analytical method has been widely used in many researches. Moreover, using X-ray diffraction measurement, not only qualitative analysis of the sample can be carried out with the accurately measured crystal structures, but also quantitative analysis can be carried out by the variation of the XRD patterns of the sample. MIL-101(Cr) is a highly crystalline porous material with periodic network structures, and XRD is performed in this study to identify its crystal structures and cell parameters. The measurement conditions used are as follows: the scanning speed is 0.1 s/step, the scanning step is 0.02 degree, and the scanning range is 2-50 degrees. The experiment measured XRD patterns of synthesized MIL-101(Cr) is shown in Figure 2-6.

From Figure 2-6, it is not difficult to find that three main diffraction peaks can be observed at 3.2, 8.4, and 9.1 degrees, which all belong to the MIL-101(Cr) crystal structures. The obtained XRD patterns are in good agreement with the previous report [65] and the simulation, indicating that the MIL-101(Cr) has intact crystal structures, and the synthesis in this study is successful. Furthermore, compared to the simulated XRD patterns, the diffraction peaks of the synthesized MIL-101(Cr) are stronger, indicating that the amount of reagents added in the synthesis process has an effect on the crystallization of the MIL-101(Cr).

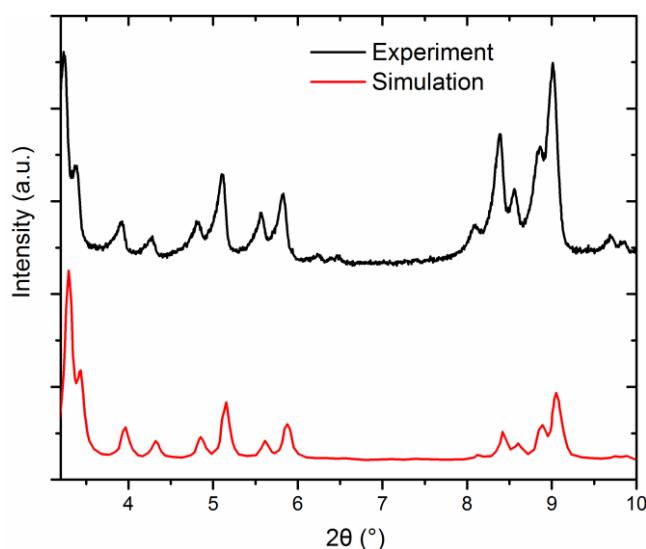


Figure 2-6 Experiment measured and simulated XRD patterns of synthesized MIL-101(Cr).

2.2.4 Raman spectroscopy for structural information

Raman spectroscopy is an analytical technique to measure the vibrational energy modes of the materials. It extracts the information through the detection of Raman scattering from the sample. When light is irradiated on molecules, it will be scattered by molecules. Most scattered light has the same frequency as the incident light, but some light fractions have different frequencies due to the interaction between the oscillation of light and molecular vibration. The phenomenon that the light is scattered with frequency change is Raman scattering. Because this frequency modulation is specific to molecular vibration and phonon in the crystal, it is possible to analyze the composition of the material or crystal structure information by analyzing this spectrum of Raman scattered light. Therefore, Raman spectroscopy has been widely used in many researches, and with the Raman spectrum, both the chemical as well as structural information of the sample and the identification of substances through its characteristic Raman region can be

determined. In this study, the Raman spectrum of the MIL-101(Cr) is measured to investigate the crystal structures and composition information of the MIL-101(Cr), as shown in Figure 2-7.

From Figure 2-7, it can be noticed that four characteristic peaks are observed at around 875, 1150, 1457, and 1616 cm^{-1} , which are consistent with the previous report [66], confirming that the desired MIL-101(Cr) crystallite is successfully synthesized. In addition, the peak appears at 472 cm^{-1} and the variation of the baseline are both caused by the Raman spectrum of the glass container.

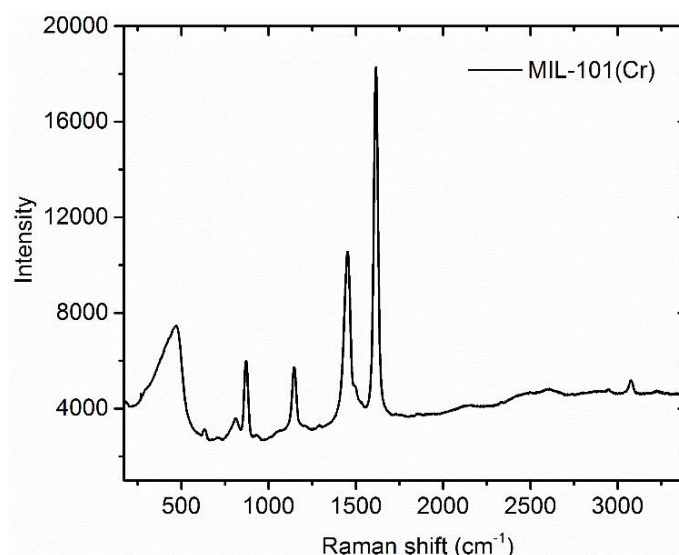


Figure 2-7 Experiment measured Raman spectrum of synthesized MIL-101(Cr).

2.2.5 Nitrogen sorption-desorption for pores properties

Advanced porous materials always contain various pore structures with the diameter in nano or micro scales, and therefore it is impossible to measure the specific surface area and pore size of these materials directly. Nitrogen sorption-desorption measurement is a commonly used method to determine the pore structure parameters of the porous

materials, including the specific surface area, pore volume, and pore size distribution. According to the multilayer adsorption theory, under a specific condition, there is a fixed equilibrium adsorption amount of the surface and by measuring this adsorption amount, the pore structure parameters of the sample can be calculated with the use of the corresponding theoretical models. N₂ sorption-desorption measurement of dehydrated MIL-101(Cr) is performed at -196°C in this study to analyze the synthesized cages structures, and the N₂ adsorption isotherm is shown in Figure 2-8.

Noticeably, the presence of the two-step uptakes at about $P/P_0 = 0.1$ and 0.2 confirm that the synthesized MIL-101(Cr) is a zeolitic mesoporous material that has two different size cages within the structures as shown in Figure 2-4. The specific surface area is calculated with the Brunauer-Emmett-Teller (BET) method [67], the total pore volume is obtained using the t-plot analysis, and the pore size distribution is gained by the nonlocal density functional theory (NLDFT) [68]. As expected, MIL-101(Cr) exhibits a large pore volume equals $2.9 \text{ cm}^3/\text{g}$ with a high specific surface area equals $3601 \text{ m}^2/\text{g}$. For the pore size distribution, there are two size cages with the diameter of 2.6 and 3.2 nm that are mainly exist in the structure of synthesized MIL-101(Cr) (see the inset of Figure 2-8), which is in agreement with the above description of its cages structures.

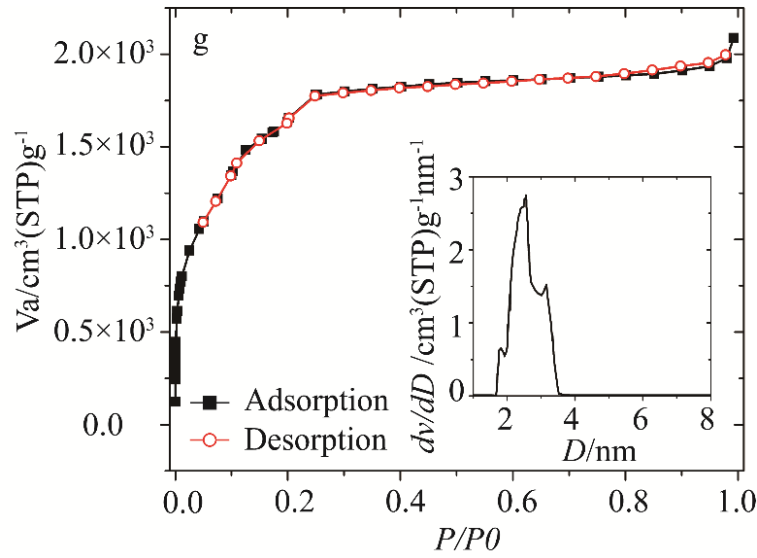


Figure 2-8 Nitrogen sorption-desorption isotherm of synthesized MIL-101(Cr) at -196°C . Inset: pore size distribution obtained by the NLDFT method.

2.2.6 Water sorption-desorption for isotherm

Water sorption-desorption isotherm [69] is a curve exhibiting the relationship between adsorbed water amount and relative humidity of the material at the equilibrium state. For each humidity value, a sorption isotherm indicates the corresponding water amount that has been absorbed within the structures of the material at the given and constant temperature. If the composition or quality of the material changes, its sorption behavior will also change, and because of the complexity of the sorption process, the isotherm cannot be precisely determined by the calculation, but it can be recorded in the corresponding water sorption-desorption measurement. As mentioned in chapter 1, to enhance the cooling efficiency and reduce the energy consumption of sorption-based AC units, MIL-101(Cr) is considered as the most suitable porous absorbent that can be used in the sorption-desorption cycle. The thermal performance of these AC units can be estimated by the amount of water loaded on the MIL-101(Cr) as determined from the

water sorption-desorption isotherm. Therefore, to help the design of the efficient sorption-based AC units, water sorption-desorption isotherm of synthesized MIL-101(Cr) at 25°C is measured in this study to first verify its water adsorption capacity, and the results are shown in Figure 2-9.

Water sorption-desorption capacity of the MIL-101(Cr) is revealed by the type-V isotherm observing in Figure 2-9 [70]. A significant water adsorption/desorption occurs in a stepwise manner within a narrow pressure variation range ($0.4 < P/P_0 < 0.5$ and $0.3 < P/P_0 < 0.4$, where P_0 is the saturated water vapor pressure equals to 3169 Pa at 25°C) in both the adsorption and desorption processes [70]. This stepwise water uptake is a result of the consecutive filling of two different mesoporous cages (29 and 34 Å in their diameters) that compose the structures of the MIL-101(Cr). The total water uptake is 1300 cm³/g, which is 2.5 to 5 times higher than that of the silica gel and zeolites [71]. A hysteresis loop is also observed between the sorption-desorption processes [68]. It is a physical process for the MIL-101(Cr) adsorbing water, and no dissociation of water will occur within the structures. The narrow stepwise manner and superior water uptake indicate that the demand for energy-saving and efficiency improvement could be satisfied using the MIL-101(Cr) as the sorption-desorption material.

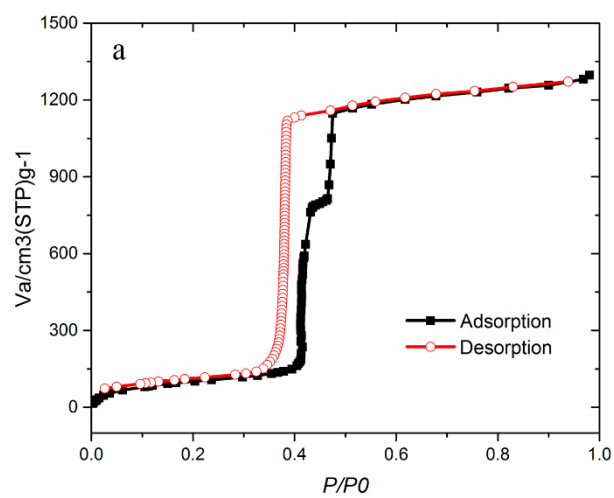


Figure 2-9 Water sorption-desorption isotherm of synthesized MIL-101(Cr) at 25°C.

Chapter 3: Diffuse reflectance infrared spectroscopy and molecular dynamics simulation

3.1 Diffuse reflectance infrared spectroscopy (DRIFTS)

Although the thermal performance of the sorption-based AC units can be estimated with the amount of water loaded on the MIL-101(Cr) as determined from water sorption-desorption isotherm, the detailed behaviors of this porous material, especially the phases of water incorporated in the matrix of the MIL-101(Cr) (confinement effect), is still not fully elucidated so that the design of efficient sorption-desorption cycle based AC units is still hampered now. Based on this problem, water phases and dynamic behaviors in the MIL-101(Cr) and two functional MIL-101(Cr) as a function of water amount at different temperatures are seriously elucidated in this study by the diffuse reflectance infrared spectroscopy and molecular dynamics simulation.

Diffuse reflectance infrared spectroscopy (DRIFTS) is a powerful method to determine the variation of the sample polymorphic forms in detail so that it has been seriously studied and widely applied in many researches. Meunier et al. discussed the checks that should be carried to ensure the kinetic and spectroscopic measurement of the DRIFTS [73]. Rieth et al. used the DRIFTS spectrum to analyze the water confined in the porous $\text{Co}_2\text{Cl}_2\text{BTDD}$ material [74]. Hunger et al. used the DRIFTS spectrum to confirm the water behaviors in the NaX material [75]. Couble et al. used the DRIFTS spectrum to study the heat of the adsorption of CO on the TiO_2 and $\text{CuO}/\text{Al}_2\text{O}_3$ materials [76]. Therefore, as the most appropriate analytical method, diffuse reflectance infrared

spectroscopy is also selected in this study to elucidate the transitions of water molecules that confined in cages structures of the MIL-101(Cr) and two functional MIL-101(Cr) to help the further development of sorption-desorption cycle based AC units.

3.1.1 Working principle of DRIFTS

For diffuse reflectance infrared spectroscopy, the working principle is shown in Figure 3-1 [77]. It can be noticed that a powdered sample is first put into a sample cell, and then an IR beam shoots to this sample. When the IR beam hits the sample powder, it can pass through or reflect by the sample surface. When passing through, the sample powder will absorb the IR radiation at different amount which only depends on the properties of this material. The transmission-reflectance events can occur many times in the sample powder, significantly increasing the path length of the measurement. Therefore, the out-coming IR beam will carry more specific adsorption information of the sample powder, and finally it will be collected by a spherical mirror and focused on a detector.

Based on this working principle, it is not difficult to find that the DRIFTS is the most suitable method for measuring the non-transparent and highly adsorbing powdered samples. Compared to the conventional infrared transmission and adsorption spectroscopy, the DRIFTS spectrum is more sensitive and can carry more adsorption information of the analytes so that the variation of their polymorphic forms can be precisely determined. Moreover, the DRIFTS spectrum has a better signal to noise ratio, and no sample preparation process is needed before the measurement.

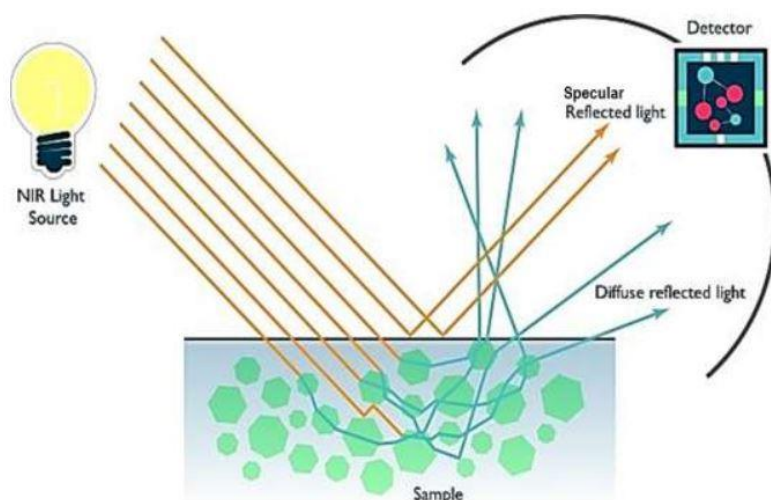


Figure 3-1 Working principle of diffuse reflectance infrared spectroscopy [77]. Reprinted with permission, Copyright © 2018, Okparanma RN, Araka PP, Ayotamuno JM, Mouazen AM.

3.1.2 Y-axis: Kubelka-Munk value

Diffuse reflectance infrared spectroscopy can provide invaluable insights into the nature and concentration of the adsorbates that are present in structures of the adsorbents. To study the properties of the material, the quantitative analysis of the DRIFTS spectrum needs to be performed, and ideally, a function of the DRIFTS intensity that is linear with the concentration of the adsorbate would be preferred [78]. In this regard, Kubelka-Munk value, which relates the diffuse reflectance to the adsorbate concentration using a scaling factor, is widely used in the y-axis to plot the DRIFTS spectrum.

The basis of the diffuse reflectance theory used to quantify the concentration of a solute in an absorbing matrix was developed by Kubelka and Munk, and this theory is simplified modeling of the diffuse reflectance considering a semi-infinite thick sample positioned on the support [76]. The Kubelka-Munk formula can be defined as:

$$f(R_{\infty}) = \frac{(1-R_{\infty})^2}{2R_{\infty}} = \frac{k}{s} \quad (1)$$

where R_{∞} is the absolute reflectance of the scattered radiation, which equals the intensity scattered divided by that of the incident radiation. s is the sample scattering coefficient, dominating the size and refractive index of the sample self so that it is considered as a constant in the K-M formula. k is the sample adsorption coefficient, which can be given by:

$$k = 2.303\epsilon C \quad (2)$$

where ϵ is the molar absorptivity and C is the solute concentration. By combining the equations (1) and (2), the following formula can be calculated as:

$$C = \text{constant} \times f(R_{\infty}) \quad (3)$$

In this formula, Kubelka-Munk function $f(R_{\infty})$ value is directly proportional to the solute concentration C , indicating that the intensity of the peaks in the DRIFTS spectrum obtained in this study is directly proportional to the water amount that adsorbed within the cages structures of the MIL-101(Cr).

3.3 Molecular dynamics simulation

Molecular dynamics (MD) simulation is a computer simulation method for analyzing the thermodynamic and dynamic properties of molecules at the atomistic level [79]. Routinely, it is used for modeling the time-dependent trajectories of molecules so that detailed information on the subtle interaction between these molecules and the confinement can be provided. The simulation of molecules motions is realized by numerically solving Newton's dynamic equations for the system, where the forces between the molecules and their potential energies are calculated using interatomic

potentials or molecular mechanics force fields [80]. With the corresponding program packages, MD simulation can be performed to investigate the structure and dynamics properties of molecules as well as their complexes and to confirm the results obtained from other analytical methods such as X-ray crystallography and nuclear magnetic resonance spectroscopy. Therefore, MD simulation has been widely used in many researches. Keupp et al. used MD simulation to analyze the “breathing” phase transformation of MOFs [81]. Han et al. used MD simulation to analyze the hydrolysis reactions and water stability of MOFs [82]. Adatoz et al. used MD simulation to predict the membrane properties that composed of MOFs [83].

In this study, to further understand the relationship between the water molecules and the MIL-101(Cr) as well as two functional MIL-101(Cr), molecular dynamics (MD) simulations with different water amounts at different temperatures are performed, and particular emphasis is given on localizing the position of the water molecules in the cages and identifying the main vibrations that contribute to the dominant peaks obtained in the DRIFTS spectra. The combination of the experimental DRIFTS spectra with the theoretical MD simulation enables a better understanding of water molecular phases and dynamics within the cages structures of the MIL-101(Cr) as well as two functional MIL-101(Cr), and therefore leads to the further development of superior materials for use in the sorption- desorption cycle based AC units.

3.3.1 Force-field parameters

The interaction of molecules and framework in MD simulation is mainly the van der Waals interaction and Coulomb interaction, which can be given by:

$$U = U_{\text{VDW}} + U_{\text{C}} \quad (4)$$

The van der Waals interaction is modeled by the Lennard-Jones (L-J) potential function [84]:

$$U_{\text{VDW}} = 4 \cdot \varepsilon_{ij} \left[\left(\frac{\sigma_{ij}}{r} \right)^{12} - \left(\frac{\sigma_{ij}}{r} \right)^6 \right] \quad (5)$$

where r is the distance between particles, ε_{ij} and σ_{ij} are parameters used to describe the intermolecular potential. The Coulombic potential function between two atoms with electric charge is modeled according to the Ewald method [81]:

$$U_{\text{C}} = U^{\text{real}} + U^{\text{rec}} \quad (6)$$

where U^{real} and U^{rec} are the components of the Coulombic potential. The definitions of them can be given by:

$$U^{\text{real}} = \sum_{i < j} q_i q_j \frac{\text{erfc}(\alpha r)}{r} \quad (7)$$

$$U^{\text{rec}} = \frac{2\pi}{V} \sum_{k \neq 0} \frac{1}{k^2} e^{-\frac{k^2}{4\alpha^2}} \left(\left| \sum_{i=1}^N q_i \cos(k \cdot r_i) \right|^2 + \left| \sum_{i=1}^N q_i \sin(k \cdot r_i) \right|^2 \right) - \sum_i \frac{\alpha}{\sqrt{\pi}} q_i^2 \quad (8)$$

where the charge of particles i and j are presented by q_i and q_j , erfc denotes the error function complement, α is a damping factor, r_i is the spatial position of particle i , k is the wavelength and V is the volume of the cell for simulation. The L-J potential function parameters and the charges of the atoms applied for the framework of the MIL-101(Cr) in MD simulation are listed in Table 3-5.

Table 3-1 L-J potential function parameters and charges of the atoms used in MD simulation.

Atom	L-J parameter		Charge (e)
	ϵk_b^{-1} (K)	σ (Å)	
O1			-0.853
O2	48.1581	3.03315	-0.574
O3			-0.438
C1			0.496
C2	47.8562	3.47299	-0.070
C3			-0.058
F1	36.4834	3.0932	-0.547
H1	7.64893	2.84642	0.108
Cr1			1.619
Cr2	7.54829	2.69319	1.350

3.3.2 Water molecule models

Depending on the water physical properties and investigated complex processes that needed to be reproduced in MD simulation, many different water models of the potential energy of interactions have been proposed [85–87].

In this study, for water sorption-desorption behaviors, the flexible SPC/E (extended simple point charge) water model is selected [88] so that the intramolecular vibration of atoms in a single water molecule can be analyzed, and the results can be compared to that obtained in the DRIFTS spectra. The coefficients used to describe the force fields inside the molecule of the flexible SPC/E model are listed in Tables 3-6.

Table 3-2 Coefficients used in flexible SPC/E model in MD simulation [88].

O–H bond stretching				H–O–H bond bending	
Type	p_0/k_B (K/Å ²)	p_1 (Å)		Type	p_0/k_B (K/rad ²)
Harmonic	533,430	1.012		Harmonic	38,226
$\epsilon_0 k_B^{-1}$ (K)	σ_O (Å)	q_O (e)	q_H (e)	l_{O-H} (Å)	Θ_{H-O-H} (deg)
78.2	3.1656	-0.8476	0.4238	1.0	109.47

3.3.3 Numerical set-up

Based on above mentioned force fields and model parameters, the configuration of water molecules in the MIL-101(Cr) and two functional MIL-101(Cr) is simulated by MD simulation on the RASPA platform under different temperatures and pressure conditions.

In MD simulation, the time step is set to 0.05 fs. With this time step, the characteristic frequency band of water intramolecular motions could be captured and the simulation time is affordable. The total simulation time is 25 ps. The ensemble is selected as canonical ensemble (NVT). The Nose-Hoover thermostat is used to keep the desired temperature of the simulated system. The periodic boundary condition is applied to the simulation cell. The translation and rotation of a water molecule are set with the same probability (equals 1.0). The water molecule number are obtained according to the experimental results. Moreover, to start the simulation from the near-equilibrium state, 1000 cycles of the initialization with the Monte Carlo method are performed first to obtain the initial configuration for the MD simulation.

3.3.4 Structural properties

3.3.4.1 Radial distribution function (RDF, $g(r)$)

The radial distribution function is calculated based on the configurations of water molecules in the framework obtained from MD simulations, which is defined as [90]:

$$\text{RDF}(r) = \frac{N(r, r+dr)}{4\pi r^2 \rho \cdot dr} \quad (9)$$

where r is the radial distance from a water molecule, $N(r, r + dr)$ refers to the number of water molecules between r and $r + dr$, and ρ is the number density of water molecules at distance r .

3.3.4.2 Order parameter (angular part, S_g)

The order parameter is applied to study the clustering structure of water molecules in the framework, which is defined as [91]:

$$S_g = \frac{3}{32} \sum_{j=1}^3 \sum_{k=j+1}^4 (\cos \varphi_{j,k} - (-\frac{1}{3}))^2 \quad (10)$$

where $\varphi_{j,k}$ is the angle formed with a central atom as i th and the other two atoms (j th, k th). The cosines of the angle (109.47°) between two center-vertex lines of a regular tetrahedron is $-1/3$.

3.3.4.3 Average hydrogen-bond number per water molecule (n_{HB})

The formation of the hydrogen bond between two water molecules is decided if the distance between the hydrogen atom from one water molecule (the proton donator) and the oxygen atom from the other water molecule (the proton acceptor) is shorter than 2.45 Å [92], and if the O-H \cdots O angle exceeds 150° [88].

3.3.5 Dynamic properties

3.3.5.1 Self-diffusion coefficient (D_s)

The self-diffusion coefficient of water in the framework is calculated by Einstein's relation based on the mean-square displacement (MSD), which is defined as [93]:

$$D_s = \lim_{t \rightarrow \infty} \frac{1}{6t} \langle [r(t) - r(0)]^2 \rangle \quad (11)$$

where t is the time, r is the position of the particle, and 0 refers to the initial state. For bulk liquid water, D_s is around 10^{-9} m²/s [89].

Chapter 4: Water adsorption and desorption behaviors in MIL-101(Cr) and functional MIL-101(Cr)

4.1 Effect of cages properties of MIL-101(Cr) on water sorption-desorption behaviors

4.1.1 Water phases and dynamic behaviors in MD simulation

To investigate the phases and dynamic behaviors of water molecules confined in the mesoporous cages and super-tetrahedron of the MIL-101(Cr) at various adsorption and desorption stages, MD simulations are first carried out in ascending order according to the number of water molecules, as shown in Figure 4-1.

When a small amount of water molecules is loaded (see Figures 4-1a and 4-1b), most of the single water molecules are preferentially attracted to the unsaturated Cr^{3+} site ($\text{H}_2\text{O}\cdots\text{Cr}$) directly, forming a stable connection stronger than that of the hydrogen bond. A few water molecules are attracted to the saturated Cr^{3+} site with a much weaker connection. As the water amount continually increases, water molecules are attracted to the unsaturated Cr-bonded water, and this type of water molecule becomes the nucleator for the formation of one-dimensional (1-D) water chains [95] ($(\text{H}_2\text{O})_n\cdots\text{H}_2\text{O}\cdots\text{Cr}$), where n is the number of the water molecules in the chain) inside the pore structure (see Figures 4-1d and 4-1e). The formation of the 1-D water chains is a simultaneous process as the water coordinate with the Cr^{3+} sites. Figure 4-2 exhibits the positions of the different sorption sites and the adsorbed water molecules at this low water amount state. In addition, although the ratio of the number of the Cr^{3+} sites between the 34 Å and 29 Å

cages is 1.4, the density of these metal sites are similar, indicating that the probability of water molecules being adsorbed in these two mesoporous cages is nearly the same at such relatively low water loadings (partial pressure of water lower than 0.0013 Pa).

When more water molecules are loaded (see Figures 4-1g and 4-1h), the 1-D water chains gathered at the nucleation point grow in length and connect, gradually forming a water monolayer on the inner surfaces of the 29 Å and 34 Å cages. This water monolayer changes the property of the cage surface from hydrophobic to hydrophilic [74], which induces the beginning of the capillary condensation stage of the water molecules inside the pore structure. As the water amount continually increases (see Figures 4-1j and 4-1k), more water molecules are bonded to the monolayer and condense inside the mesoporous cages until the pore structure in the MIL-101(Cr) are filled. Noticeably, the 29 Å cages are always filled before the 34 Å cages at such relatively high water loadings (partial pressure of water higher than 0.0013 Pa), as the inner surface of the 29 Å cage is smaller and the curvature is larger. Therefore, the 1-D water chains easily connect, and the water monolayer forms first in the 29 Å cage, leading to a large amount of water first condense in this medium cage. Although a filling sequence of the two cage types is found in the simulation, only a slight difference in the partial pressure of water can be observed in the isotherm when the capillary condensation occurs in the 29 Å and 34 Å cages. That is because the difference between the pore diameters and the curvatures of these two cages is not so significant.

Note that during the filling process of the 29 Å and 34 Å cages, only a few water molecules move into the super-tetrahedrons (see Figures 4-1c, 4-1f, 4-1i, and 4-1l). These water molecules are not as stable as those in the mesoporous cages because the framework

of this 8 Å structure is small and will lead to a strong repulsion force to the adjacent water molecules [96]. When a large amount of water is loaded, all the super-tetrahedrons in the MIL-101(Cr) will also be filled. Although the number of the inside water molecules in one 8 Å super-tetrahedron structure is no more than five, they still may result in a slight increase in the isotherm when the partial pressure of water is higher than 0.0019 Pa. In addition, no interaction of water molecules with the carboxylate is found in the MIL-101(Cr) [97].

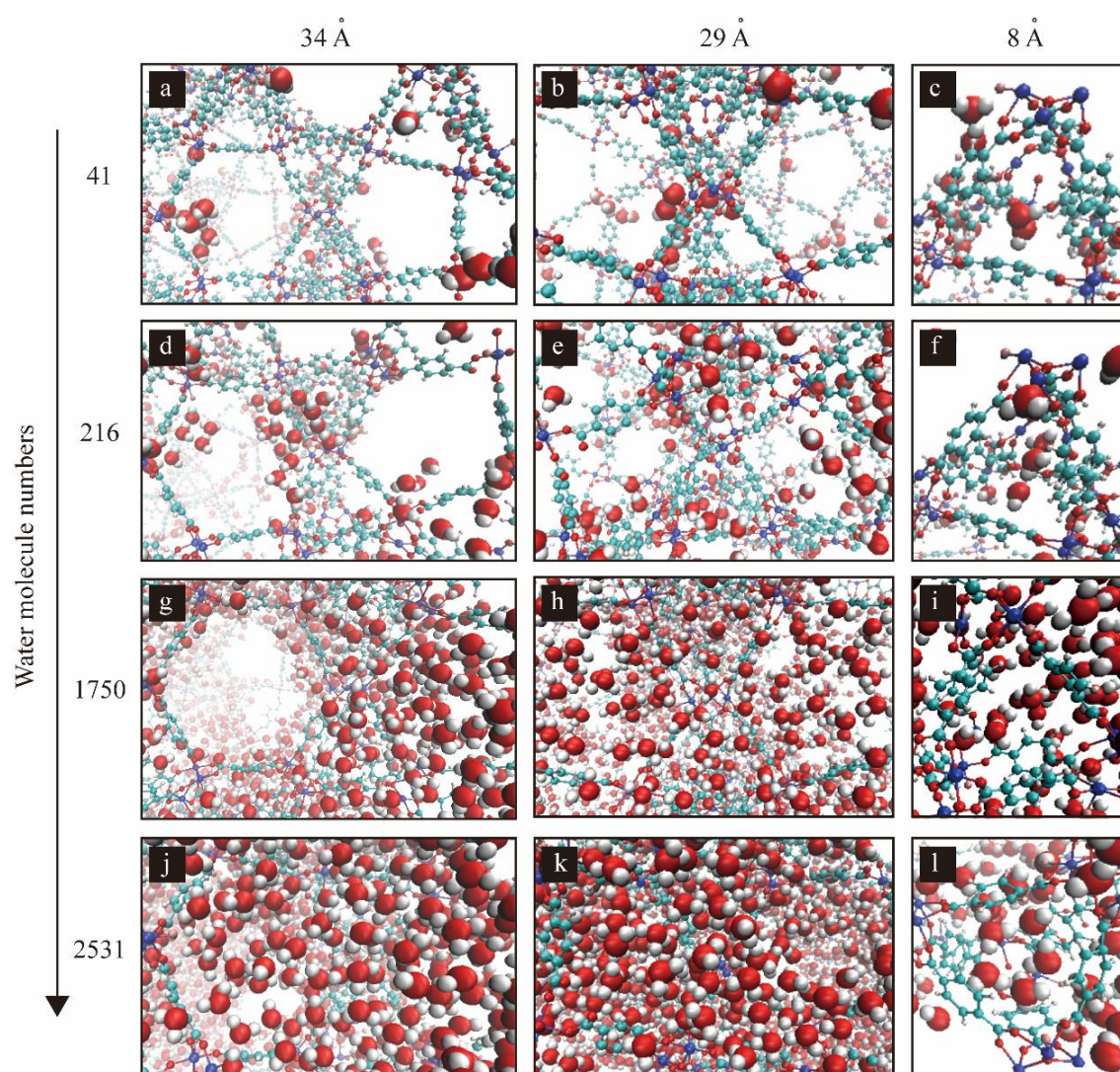


Figure 4-1 Phases and dynamic behaviors of water molecules in the 34 Å and 29 Å cages, and 8 Å super-tetrahedron of the MIL-101(Cr) simulated by MD simulation with (a-c) 41, (d-f) 216, (g-i) 1750, and (j-l) 2531 water molecules. The Cr, C, O, H, and F atoms are in navy, blue, red, white, and pink, respectively.

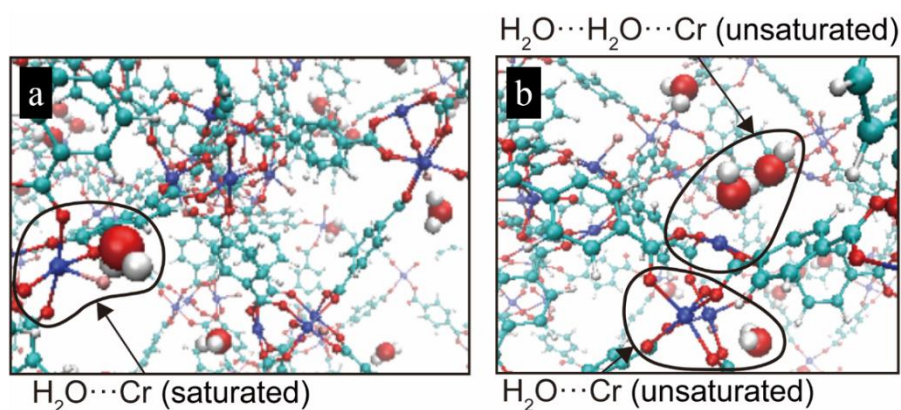


Figure 4-2 Different water sorption sites in MD simulation when only a small amount of water molecules is loaded: (a) Saturated Cr^{3+} site. (b) Unsaturated Cr^{3+} site and unsaturated Cr-bonded water.

4.1.2 Water phases in DRIFTS spectra

DRIFTS spectra at various sorption-desorption stages are recorded as shown in Figure 4-3 to analyze the phases and dynamic behaviors of water molecules in the MIL-101(Cr). Significant variations corresponding to molecular adsorption in the spectra are observed between 3100 and 3800 cm^{-1} . This region corresponds to the OH stretching band [98], thus indicating that water molecules experience an interplay with the pore structure of the MIL-101(Cr) in the sorption-desorption processes. Figure 4-4a exhibits the DRIFTS spectra of the MIL-101(Cr) at 6 Pa in the OH stretching region, where two peaks around 3586 and 3672 cm^{-1} are significant. To illustrate the main water vibrations

contributing to these two peaks, the vibration frequency spectra of water molecules are calculated using the MD simulation.

Figure 4-4b shows the calculated vibration frequency spectrum of each of the 41 water molecules (lower figure, each color line represents one water molecule) in the simulation and the sum of all the spectra (upper figure, in green). Similarly, Figure 4-4c shows the calculated vibration frequency spectrum of each of the 216 water molecules (lower figure, each color line represents one water molecule) in the simulation and also the sum of all the spectra (upper figure, in blue). As shown in Figures 4-4b and 4-4c, the vibration frequency of water molecules can be divided into two parts: 106-109 THz and 109-111 THz, exactly corresponding to the two sharp peaks obtained in the DRIFTS spectrum. For the vibration frequency in the range of 106-109 THz, the position of the related water molecules are located within the pores of the MIL-101(Cr) in the simulation, and these frequency peaks are found to be caused by the single water molecules coordinated with the Cr^{3+} sites ($\text{H}_2\text{O}\cdots\text{Cr}$). Figure 4-4d exhibits the vibration frequency of two water molecules coordinated with the saturated and unsaturated Cr^{3+} sites, respectively. The insets show the relative physical position between this type of water molecules and the Cr^{3+} sites. The result indicates that the vibration frequency of the single water molecules bonded to the unsaturated Cr^{3+} site is slightly higher than that bonded to the saturated Cr^{3+} site. For the vibration frequency in the range of 109-111 THz, the related water molecules are located in the simulation, and these frequency peaks always correspond to the first water molecules that coordinated with the unsaturated Cr^{3+} sites in the 1-D water chains $((\text{H}_2\text{O})_n\cdots\text{H}_2\text{O}\cdots\text{Cr})$. The vibration frequency of the first water molecule in the water chains for the 29 Å and 34 Å cages are compared in Figure 4-4e.

The insets illustrate the relative physical position of these water molecule chains in the two cages types. Similarly, a difference in the vibration frequency between the first water molecule in the water chain for the 29 Å and 34 Å cages is observed. These reveal that the different surrounding conditions, such as the saturated or unsaturated Cr^{3+} sites and the different sizes of the cages, will lead to a variation of the total confinement effect of the water molecules, slightly varying their vibration frequency in each range. In addition, when a small amount of water molecules is loaded, there are more peaks in the 106-109 THz and as the water amount increases, the peaks in the 109-111 THz gradually increase. This is in agreement with our previous description of water molecules preferentially coordinating with the Cr^{3+} sites at the beginning and gradually forming the 1-D water chains inside the pores when the water amount increases.

Noticeably, the vibration frequency of the water molecules coordinated with the Cr^{3+} sites shifts to a higher value when additional water molecules bond and form the water chains. It seems that when the adsorption state changes from the $\text{H}_2\text{O} \cdots \text{Cr}$ to the $(\text{H}_2\text{O})_n \cdots \text{H}_2\text{O} \cdots \text{Cr}$, the confinement effect on the Cr-bonded water molecule may vary significantly, which would limit the stretch vibration of the molecule and decrease its motion amplitude, leading to a higher main vibration frequency. Except for the first water molecules coordinated with the unsaturated Cr^{3+} sites, the vibration frequency spectra of other water molecules in the 1-D water chains are also analyzed as shown in Figure 4-5. The vibration of the second and the third water molecules become irregular, and there seems no significant dominant vibration frequency compared to the first water molecule that is bonded to Cr^{3+} in the chain. Moreover, when the number of water molecules in the

chain increases, the vibration of other water molecules broaden the peaks and form a tail around 3709 cm^{-1} in the spectra.

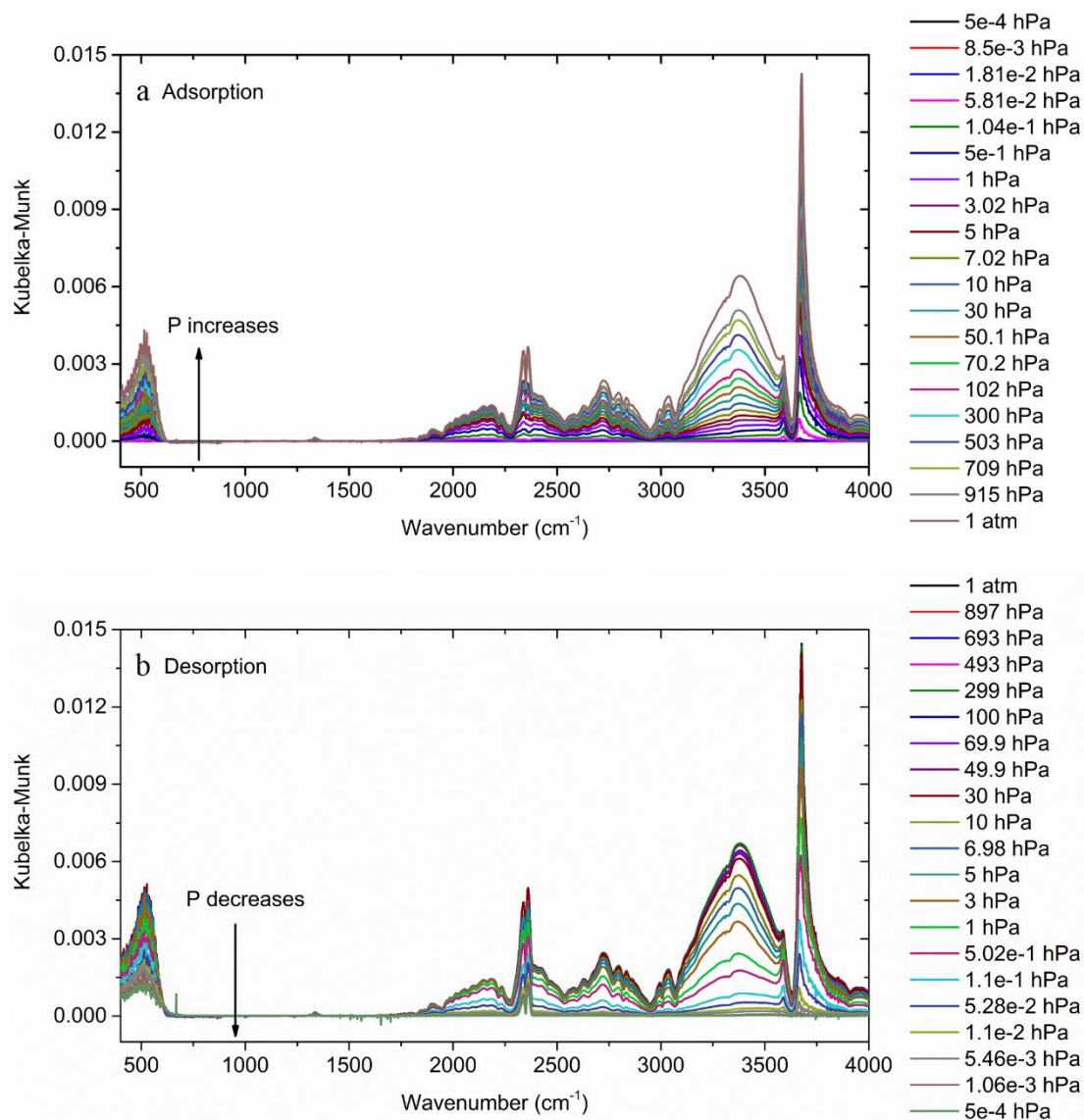


Figure 4-3 Variation of DRIFTS spectra of the MIL-101(Cr) at different air pressures (P_{air}) in (a) adsorption and (b) desorption processes.

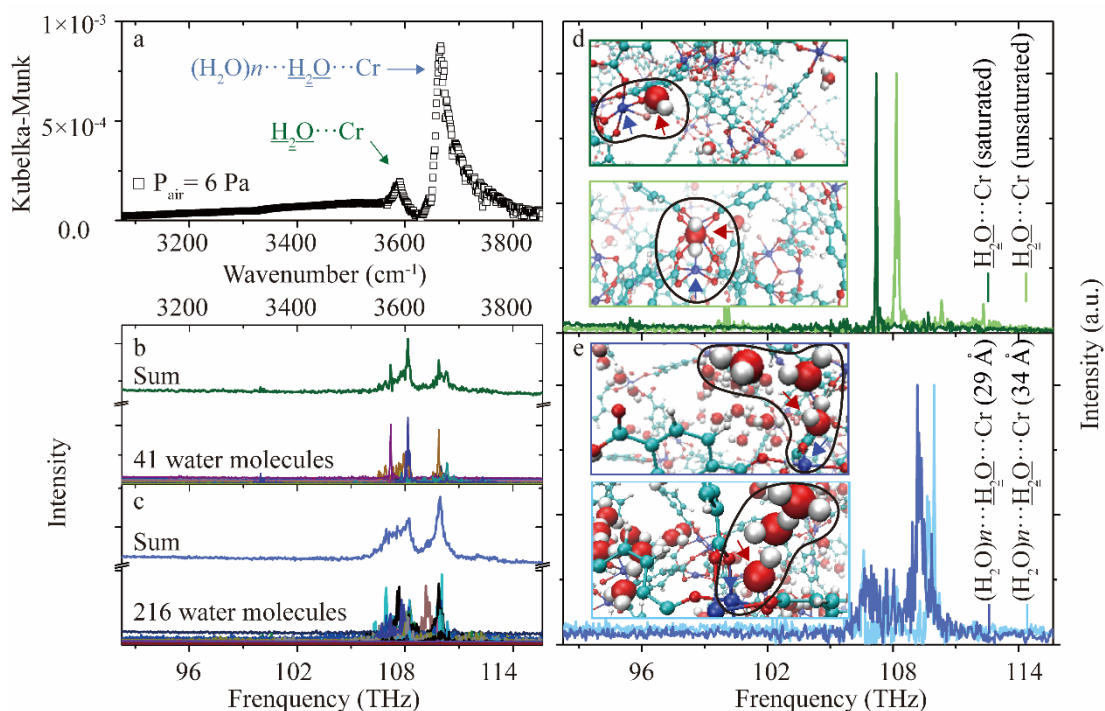


Figure 4-4 (a) DRIFTS spectrum of $\text{H}_2\text{O} \cdots \text{Cr}$ and $(\text{H}_2\text{O})_n \cdots \text{H}_2\text{O} \cdots \text{Cr}$ in the MIL-101(Cr) at 6 Pa (P_{air}). MD simulated vibration frequency spectra for (b) the 41 water molecules (lower figure, each color line represents one water molecule) as well as the sum of all spectra (upper figure, in green), and (c) the 216 water molecules (lower figure, each color line represents one water molecule) as well as the sum of all spectra (upper figure, in blue). MD simulated vibration frequency spectra of (d) single water molecule coordinated with the saturated (dark color) and unsaturated Cr^{3+} sites (light color), and (e) the first water molecule in the water chains for the 29 Å (dark color) and 34 Å cages (light color). Insets: positions of two types of water molecules in the two cages of the MIL-101(Cr). The Cr, C, O, H, and F atoms are in navy, blue, red, white, and pink, respectively.

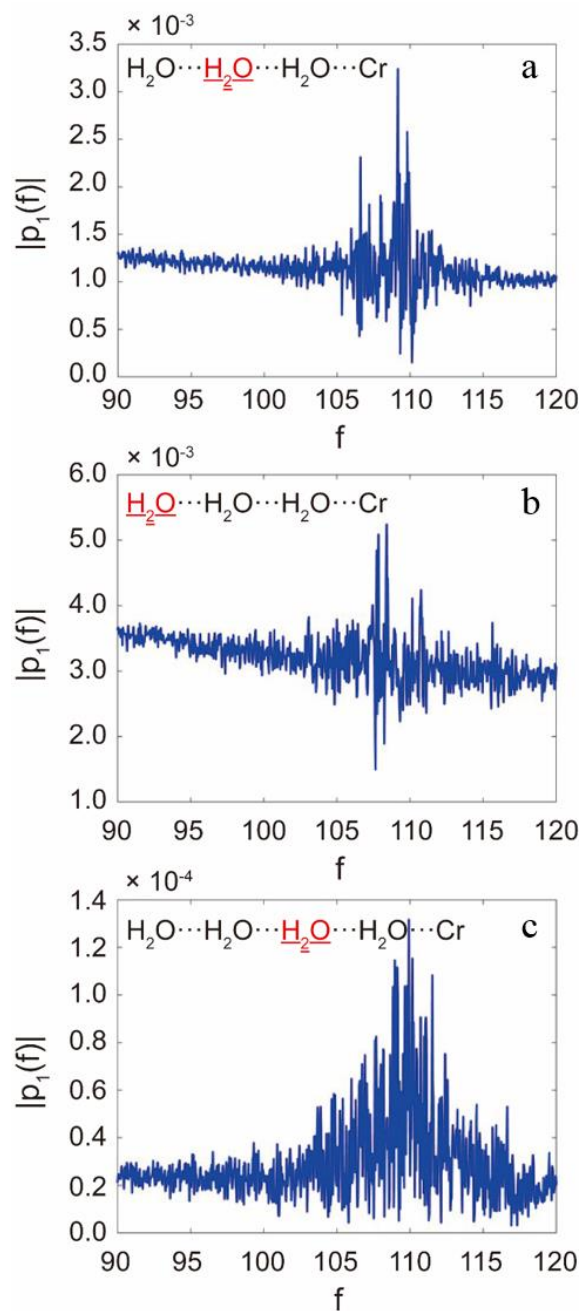


Figure 4-5 MD simulated vibration frequency spectra of water molecules (in red with underline) in the 1-D water chains: (a) Second water molecule in a three-water-molecule chain. (b) Third water molecule in a three-water-molecule chain. (c) Second water molecule in a four-water-molecule chain.

The DRIFTS spectra of the MIL-101(Cr) with increased air pressures are shown in Figure 4-6. Except for the two peaks described above, a broad peak in the OH stretching region is also observed. For a pressure higher than 500 Pa, the broad peak around 3416 cm^{-1} becomes predominant, indicating a gradual filling by water molecules of the MIL-101(Cr) pores.

The appearance of the broad peak is in agreement with other reports [99], which is attributed to the formation of liquid-like water in the MIL-101(Cr). The DRIFTS spectrum of this broad peak in the OH stretching region is compared to that of the bulk water at 25°C (see Figure 4-7). In general, the spectrum of bulk water can be well fitted with three Gaussian components [100]: the lowest frequency Gaussian represents highly confined water molecules having an H-bond coordination number close to four, the middle frequency Gaussian represents the intermediate water having a coordination number close to three, and the highest frequency Gaussian represents the loosely bonded water having an H-bond coordination number less than three. It is worth noticing that the water molecules confined in the MIL-101(Cr) exhibit a similar peak shape as that of the bulk water. This confirms that liquid-like water is present within the pores of the MIL-101(Cr) in the latter half of the filling process [61] as predicted by the MD simulation, where the 29 Å and 34 Å cages are found to be gradually filled with condensed water as pressure increases. All characteristic peaks analyzed above are summarized in Table 4-1 in descending order according to the number of water molecules.

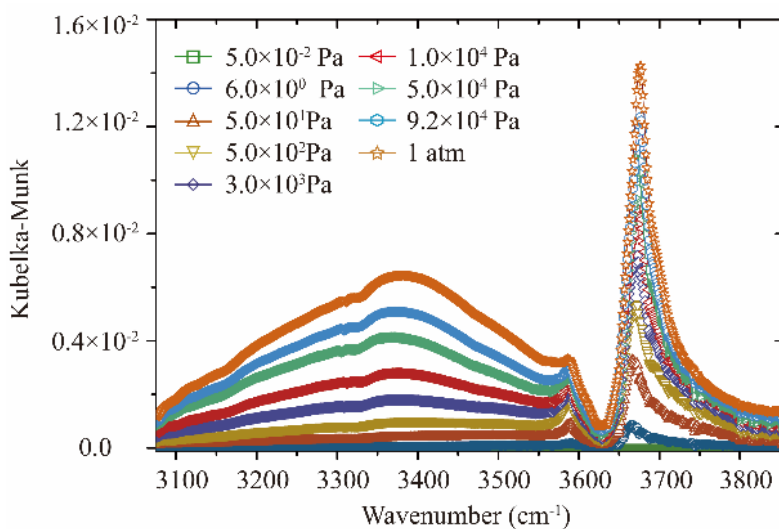


Figure 4-6 Variation of DRIFTS spectra of the liquid-like water in the MIL-101(Cr) with the increased air pressures.

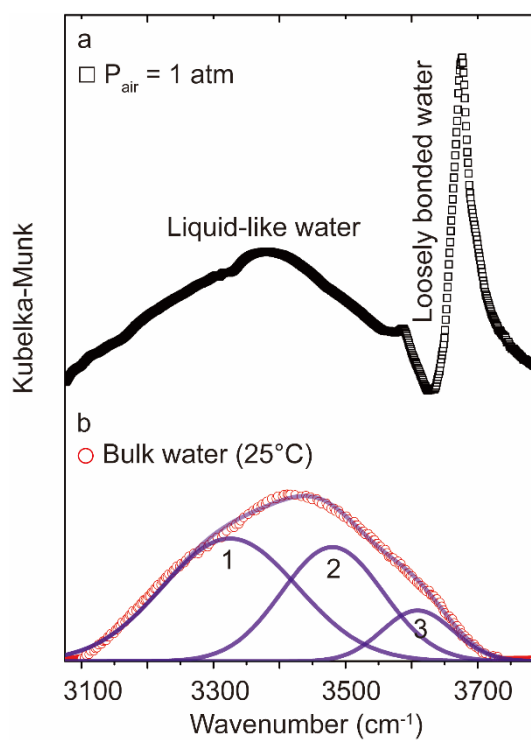


Figure 4-7 (a) DRIFTS spectrum of liquid-like water in the MIL-101(Cr) at 1 atm (P_{air}).
(b) Infrared spectrum of bulk water at 25°C with three Gaussian components [100].

Table 4-1 Characteristic DRIFTS peaks of different types of water in the MIL-101(Cr).

Wavenumber (cm ⁻¹)	Water types	Wavenumber (cm ⁻¹)	Water types
3269 (G1)	highly combined water (four H-bonds)	3709 (G6)	^a (<u>H₂O</u>) _n ···H ₂ O···Cr (other water molecules in the water chain)
3416 (G2)	Intermediate water (three H-bonds)	3674 (G5)	(H ₂ O) _n ··· ^a <u>H₂O</u> ···Cr (the first water molecule in the water chain)
3527 (G3)	Loosely bonded water (two, one, or zero H- bonds)	3584 (G4)	^a <u>H₂O</u> ···Cr (a single water molecule bonded to Cr ³⁺)

^a Underlined H₂O indicates the dominant contribution to the corresponding peak in the DRIFTS spectra.

4.1.3 Water dynamic behaviors in DRIFTS spectra

To further elucidate the transition of different types of water molecules within the MIL-101(Cr), DRIFTS spectra recorded at different air pressures are fitted with six independent Gaussian functions centered at 3269 (G1), 3416 (G2), 3527 (G3), 3584 (G4), 3670 (G5), and 3709 (G6) cm⁻¹, respectively, as shown in Figures 4-8a to 4-8f for the adsorption process and 4-8h to 4-8m for the desorption process. The relative area ratio of each component is presented in the insets and the area variation of the six components is summarized in Figures 4-8g and 4-8n.

For the adsorption process, when a small amount of water is loaded (see Figure 4-8a), the G4, G5, and G6 components contribute to about 70% of the spectrum, implying that the favorable location of the water molecules at the initial stage is to directly coordinate with the Cr^{3+} sites and form 1-D water chains inside the pore structure. With the increase in the pressure (see Figures 4-8b, 4-8c, and 4-8d), the G3, G2, and G1 components increase in sequence until the contribution becomes close to that of the G4, G5, and G6 components. This phenomenon reveals the transition of water types from single water molecules bonded to Cr^{3+} and 1-D water chains to the water monolayer on the inner surfaces of the 29 Å and 34 Å cages, indicating that the confined water molecules gradually increase in the MIL-101(Cr). As pressure increases to the maximum value of 1 atm (see Figures 4-8e and 4-8f), G1 becomes the largest component, and the proportion of the G1, G2, and G3 components exceeds that of the G4, G5, and G6 components, contributing to 72% of the spectrum. At that stage, the distribution of the broad peak shape is similar to that of the bulk water, implying that the water layers along the inner surface of cages become thick, and the pores inside the MIL-101(Cr) are filled with the condensed water. Similar dynamic behaviors of water molecules can also be confirmed from the area variation of each component, as the areas of G4, G5, and G6 components increase first, while the areas of the G1, G2, and G3 components vary significantly when the pressure is larger than 3000 Pa (see Figure 4-8g).

For the desorption process, when the pressure decreases from 1 atm (see Figures 4-8h, 4-8i, and 4-8j), the highly confined water, typically represented by the condensed water that filled in the 29 Å and 34 Å cages, are gradually desorbed from the MIL-101(Cr) as evidenced by the decrease in the G1, G2, and G3 components. Although these three

components decrease, they still contribute more to the spectrum than other components at this stage. With the decrease in the pressure (see Figures 4-8k and 4-8l), the G5 and G6 components increase, suggesting that the confined water molecules in the thick water layer are gradually desorbed from the pore structure, and the 1-D water chains become the main existing form of water molecules inside the MIL-101(Cr). The G3 component also slightly increases at this stage, as it represents the loosely bonded water with the H-bond coordination number less than three in the liquid-like water region. As pressure continually decreases (see Figure 4-8m), the dominant G4, G5, and G6 components begin to decrease. This represents the last stage of the desorption process, where all the water molecules, including the single water molecule coordinated with the Cr^{3+} site, are desorbed from the MIL-101(Cr). The area variation of the six components reveals the similar dynamic behaviors of the water molecules being desorbed from the MIL-101(Cr). As shown in Figure 4-8n, the confined water molecules represented by the G1, G2, and G3 components are desorbed at the beginning, followed by the G4, G5, and G6 components which correspond to the 1-D water chains and the water molecules bonded to Cr^{3+} .

In addition, the spectrum does not recover to the original position when the pressure decreases to the same value as the pore filling process, indicating that there is a hysteresis between the adsorption and desorption processes (see Figure 4-9). This is in agreement with the isotherm that the desorption pressure is always smaller than the adsorption pressure when the water amount in the MIL-101(Cr) is the same.

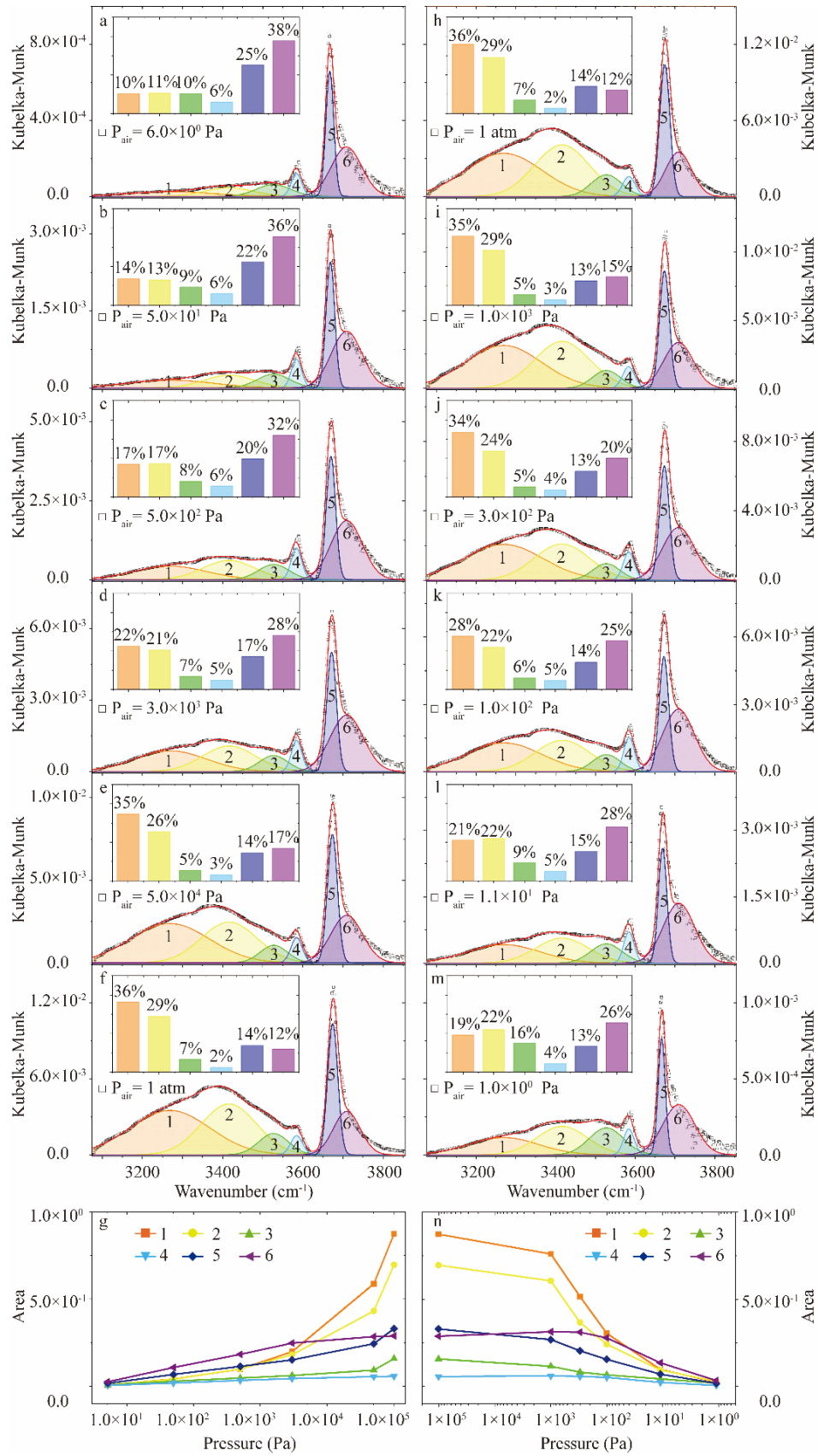


Figure 4-8 Deconvolution of the DRIFTS spectra with six Gaussian components for the air pressures of (a) 6 Pa, (b) 50 Pa, (c) 500 Pa, (d) 3000 Pa, (e) 50000 Pa, and (f) 1 atm. (g) Area variation of six Gaussian components in the adsorption process (log scale for the x -axis). Deconvolution of the DRIFTS spectra with six Gaussian components for the air pressures of (h) 1 atm, (i) 1000 Pa, (j) 300 Pa, (k) 100 Pa, (l) 11 Pa, and (m) 1 Pa. (n) Area variation of six Gaussian components in the desorption process (log scale for the x -axis). Insets: relative area ratios of each component at each pressure.

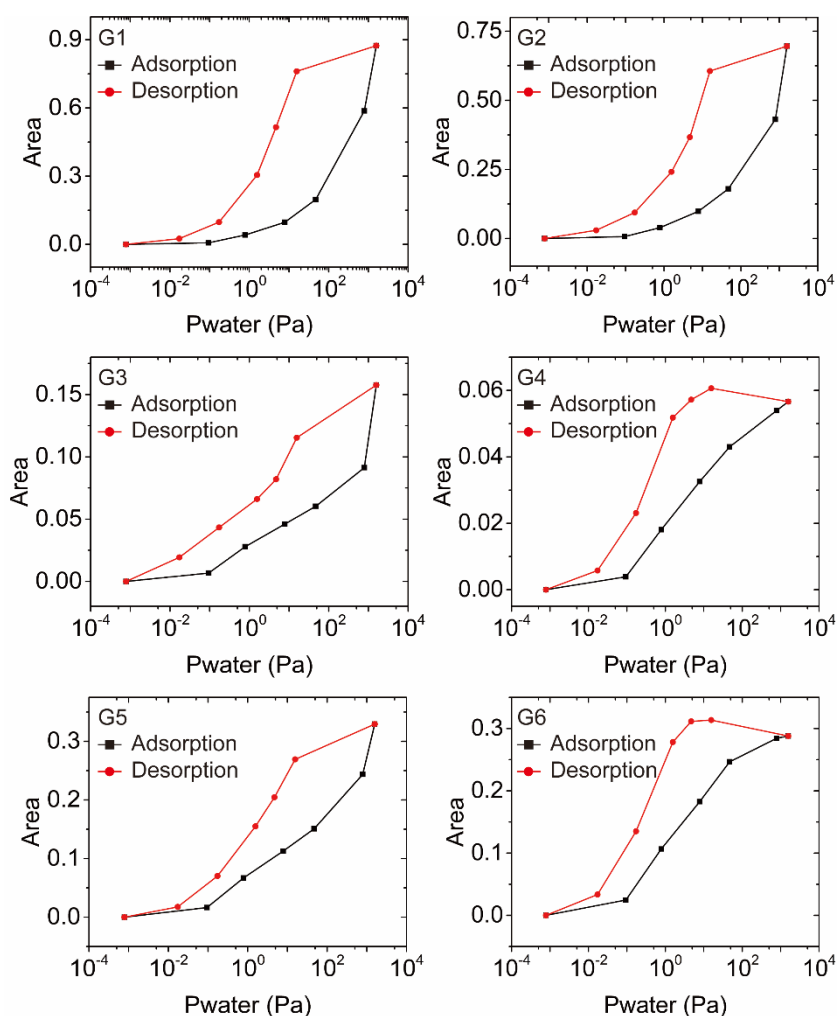


Figure 4-9 Hysteresis between the adsorption and desorption processes of six Gaussian components (from G1 to G6).

Chapter 6: Conclusions and future Work

The goal of this thesis is to study the phases and dynamic behaviors of water molecules adsorbed in the MIL-101(Cr), MIL-101(Cr)-SO₃H, and MIL-101(Cr)-NO₂. In particular, the confinement effect of cages structures, the bonding position of water molecules, and the different types of water molecules at different sorption-desorption stages are the major areas of focus for this thesis.

In the pursuit of this goal, MIL-101(Cr) and two functional MIL-101(Cr) are first prepared using the reported hydrothermal reaction. The morphology of synthesized MIL-101(Cr) shows that it is a solid material that has a regular octahedral structure with smooth surfaces. The XRD patterns and Raman spectra of the MIL-101(Cr) are found to be in good agreement with the previous reports and simulation results, indicating that the desired MIL-101(Cr) crystallite is successfully synthesized. The N₂ adsorption isotherm confirms that the MIL-101(Cr) has two different size cages with diameters of 2.6 and 3.2 nm in the structures, and it exhibits a large pore volume equals to 2.9 cm³/g with a large specific surface area equals to 3601 m²/g. MIL-101(Cr) processes a type-V isotherm, and a significant water adsorption/desorption occurs in a stepwise manner within a narrow pressure variation range. The total water uptake of it is 1.3 g/g. which is 2.5 to 5 times higher than that of the conventional zeolites and silica gel.

DRIFTS, which can carry more information of the powdered analytes and determine their polymorphic forms, is selected to be used. To further confirm the phenomena that have been found in DRIFTS spectra, MD simulations under the same conditions as experiments are performed, and particular emphasis is given on localizing the position of

water molecules and identifying the main vibrations that contribute to the dominant peaks. The results show that water molecules confined in the MIL-101(Cr) and two functional MIL-101(Cr) exhibit unique phases and dynamic behaviors at various sorption-desorption stages. For the original MIL-101(Cr), in the adsorption process, the water molecules first coordinate with metal sites and form 1-D water chains from the unsaturated Cr^{3+} . As the water amount increases, the 1-D water chains grow in length and connect together, gradually forming a water monolayer on the inner surfaces of the cages. This monolayer changes the property of the surface from hydrophobic to hydrophilic, which induces the beginning of water condensation in the medium and large cages. The entire pores are filled with condensed water in the end. In the desorption process, a reverse process is observed with hysteresis. The condensed water is first desorbed from the structures, followed by the water monolayer, and finally the 1-D water chains as well as single water molecule bonded to the Cr^{3+} site are desorbed from the MIL-101(Cr).

This work clearly demonstrates the phases and dynamic behaviors of water molecules confined in the MIL-101(Cr), MIL-101(Cr)-SO₃H, and MIL-101(Cr)-NO₂. The strong water peaks obtained in the DRIFTS spectra, as well as the reverse process observed with hysteresis, confirm the possible applications of these three materials, and all these systematic analyses suggest the further development of superior materials of high-efficiency sorption-desorption cycle based AC units.

References

- [1] Zheng J, Vemuri RS, Estevez L, Koech PK, Varga T, Camaioni DM, et al. Pore-engineered metal-organic frameworks with excellent adsorption of water and fluorocarbon refrigerant for cooling applications. *J Am Chem Soc* 2017;139:10601-4.
- [2] Lenzen D, Zhao J, Ernst S-J, Wahiduzzaman M, Ken Inge A, Fröhlich D, et al. A metal-organic framework for efficient water-based ultra-low-temperature-driven cooling. *Nat Commun* 2019;10:3025.
- [3] Sivak M. Potential energy demand for cooling in the 50 largest metropolitan areas of the world: Implications for developing countries. *Energy Policy* 2009;37:1382-4.
- [4] Isaac M, van Vuuren DP. Modeling global residential sector energy demand for heating and air conditioning in the context of climate change. *Energy Policy* 2009;37:507-21.
- [5] Ürge-Vorsatz D, Cabeza LF, Serrano S, Barreneche C, Petrichenko K. Heating and cooling energy trends and drivers in buildings. *Renew Sustain Energy Rev* 2015;41:85-98.
- [6] International Energy Agency (IEA). The future of cooling opportunities for energy-efficient air conditioning. IEA;Paris;2018;<https://www.iea.org/reports/the-future-of-cooling>.
- [7] Henninger SK, Schmidt FP, Henning H-M. Water adsorption characteristics of novel materials for heat transformation applications. *Appl Therm Eng* 2010;30:1692-702.

- [8] Daou K, Wang RZ, Xia ZZ. Desiccant cooling air conditioning: a review. *Renew Sustain Energy Rev* 2006;10:55-77.
- [9] Mitukiewicz G, Wozniak M, Madziara S, Najbert S, Kubiak P, Ozuna G, De La Fuente P. Engine Cooling System with Energy Recuperation. *Machines Technologies Materials* 2015;9(8):57-59.
- [10] Mon M, Bruno R, Ferrando-Soria J, Armentano D, Pardo E. Metal-organic framework technologies for water remediation: towards a sustainable ecosystem. *J Mater Chem A* 2018;6:4912-47.
- [11] Canivet J, Fateeva A, Guo Y, Coasne B, Farrusseng D. Water adsorption in MOFs: fundamentals and applications. *Chem Soc Rev* 2014;43:5594-617.
- [12] Logan MW, Langevin S, Xia Z. Reversible atmospheric water harvesting using metal-organic frameworks. *Sci Rep* 2020;10:1492.
- [13] Küsgens P, Rose M, Senkovska I, Fröde H, Henschel A, Siegle S, et al. Characterization of metal-organic frameworks by water adsorption. *Microporous Mesoporous Mater* 2009;120:325-30.
- [14] Liu Z, Chen Y, Sun J, Lang H, Gao W, Chi Y. Amine grafting on coordinatively unsaturated metal centers of MIL-101Cr for improved water absorption characteristics. *Inorganica Chim Acta* 2018;473:29-36.
- [15] Ehrenmann J, Henninger SK, Janiak C. Water adsorption characteristics of MIL-101 for heat-transformation applications of MOFs. *Eur J Inorg Chem* 2011;2011:471-4.
- [16] Catafesta J, Alabarse F, Levelut C, Isambert A, Hébert P, Kohara S, et al. Confined H₂O molecules as local probes of pressure-induced amorphisation in faujasite. *Phys Chem Chem Phys* 2014;16:12202-8.

- [17] Chandrasekhar S, Pramada PN. Thermal studies of low silica zeolites and their magnesium exchanged forms. *Ceram Int* 2002;28:177-86.
- [18] Rege SU, Yang RT, Qian K, Buzanowski MA. Air-prepurification by pressure swing adsorption using single/layered beds. *Chem Eng Sci* 2001;56:2745-59.
- [19] Jänchen J, Ackermann D, Stach H, Brösicke W. Studies of the water adsorption on Zeolites and modified mesoporous materials for seasonal storage of solar heat. *Sol Energy* 2004;76:339-44.
- [20] Wang DC, Xia ZZ, Wu JY. Design and performance prediction of a novel zeolite-water adsorption air conditioner. *Energy Convers Manag* 2006;47:590-610.
- [21] Myat A, Kim Choon N, Thu K, Kim Y-D. Experimental investigation on the optimal performance of Zeolite–water adsorption chiller. *Appl Energy* 2013;102:582-90.
- [22] Huang HY, Ito S, Watanabe F, Hasatani M, Kobayashi N. Microwave irradiation effect in water-vapor desorption from zeolites. *Microw heating* 2011; 335.
- [23] Courbon E, D’Ans P, Permyakova A, Skrylnyk O, Steunou N, Degrez M, et al. A new composite sorbent based on SrBr_2 and silica gel for solar energy storage application with high energy storage density and stability. *Appl Energy* 2017;190:1184-94.
- [24] Ng KC, Chua HT, Chung CY, Loke CH, Kashiwagi T, Akisawa A, et al. Experimental investigation of the silica gel-water adsorption isotherm characteristics. *Appl Therm Eng* 2001;21:1631-42.
- [25] C.Zhao JGY. Development of desiccants made from natural material. *Chem Ind Eng* 2005;22:56-61.

- [26] Chua HT, Ng KC, Wang W, Yap C, Wang XL. Transient modeling of a two-bed silica gel-water adsorption chiller. *Int J Heat Mass Transf* 2004;47:659-69.
- [27] Saha BB, Chakraborty A, Koyama S, Aristov YI. A new generation cooling device employing CaCl_2 -in-silica gel–water system. *Int J Heat Mass Transf* 2009;52:516-24.
- [28] Chujo Y, Saegusa T. Organic polymer hybrids with silica gel formed by means of the sol-gel method BT-macromolecules: Synthesis, order and advanced properties, Berlin, Heidelberg: Springer Berlin Heidelberg; 1992, p. 11-29.
- [29] Huber L, Comesaña SP, Koebel MM. The influence of the ammonia concentration and the water content on the water sorption behavior of ambient pressure dried silica xerogels. *J Sol-Gel Sci Technol* 2020;96:197-206.
- [30] Mileo PGM, Ho Cho K, Park J, Devautour-Vinot S, Chang J-S, Maurin G. Unraveling the water adsorption mechanism in the mesoporous MIL-100(Fe) metal-organic framework. *J Phys Chem C* 2019;123:23014-25.
- [31] Cao R, Chen Z, Chen Y, Idrees KB, Hanna SL, Wang X, et al. Benign integration of a Zn-azolate metal-organic framework onto textile fiber for ammonia capture. *ACS Appl Mater Interfaces* 2020;12:47747-53.
- [32] Salazar JM, Weber G, Simon JM, Bezverkhyy I, Bellat JP. Characterization of adsorbed water in MIL-53(Al) by FTIR spectroscopy and ab-initio calculations. *J Chem Phys* 2015;142:124702.
- [33] Coudert F-X, Ortiz AU, Haigis V, Bousquet D, Fuchs AH, Ballandras A, et al. Water adsorption in flexible gallium-based MIL-53 metal-organic framework. *J Phys Chem C* 2014;118:5397-405.

- [34] Rezk A, AL-Dadah R, Mahmoud S, Elsayed A. Investigation of Ethanol/metal organic frameworks for low temperature adsorption cooling applications. *Appl Energy* 2013;112:1025-31.
- [35] Dey C, Kundu T, Biswal BP, Mallick A, Banerjee R. Crystalline metal-organic frameworks (MOFs): Synthesis, structure and function. *Acta Crystallogr Sect B Struct Sci Cryst Eng Mater* 2014;70:3-10.
- [36] Yaghi OM, Li G, Li H. Selective binding and removal of guests in a microporous metal-organic framework. *Nature* 1995;378:703-6.
- [37] Li H, Eddaoudi M, O'Keeffe M, Yaghi OM. Design and synthesis of an exceptionally stable and highly porous metal-organic framework. *Nature* 1999;402:276-9.
- [38] Eddaoudi M, Kim J, Rosi N, Vodak D, Wachter J, Yaghi OM. Systematic design of pore size and functionality in ioreticular MOFs and their application in methane storage. *Science* 2002;295:469.
- [39] Park KS, Ni Z, Côté AP, Choi JY, Huang R, Uribe-Romo FJ, et al. Exceptional chemical and thermal stability of zeolitic imidazolate frameworks. *Proc Natl Acad Sci* 2006;
- [40] Férey G, Mellot-Draznieks C, Serre C, Millange F, Dutour J, Surblé S, Margiolaki I. A chromium terephthalate-based solid with unusually large pore volumes and surface area. *Science* 2005;309:2040 LP - 2042.
- [41] Seo J, Matsuda R, Sakamoto H, Bonneau C, Kitagawa S. A pillared-layer coordination polymer with a rotatable pillar acting as a molecular gate for guest molecules. *J Am Chem Soc* 2009;131:12792-800.

- [42] Yuan D, Zhao D, Sun D, Zhou H-C. An isorecticular series of metal-organic frameworks with dendritic hexacarboxylate ligands and exceptionally high gas-uptake capacity. *Angew Chemie Int Ed* 2010;49:5357-61.
- [43] Katz MJ, Brown ZJ, Colón YJ, Siu PW, Scheidt KA, Snurr RQ, et al. A facile synthesis of UiO-66, UiO-67 and their derivatives. *Chem Commun* 2013;49:9449-51.
- [44] Xie Q, Li Y, Lv Z, Zhou H, Yang X, Chen J, et al. Effective adsorption and removal of phosphate from aqueous solutions and eutrophic water by Fe-based MOFs of MIL-101. *Sci Rep* 2017;7:3316.
- [45] Wang P, Li X, Zhang P, Zhang X, Shen Y, Zheng B, et al. Transitional MOFs: exposing metal sites with porosity for enhancing catalytic reaction performance. *ACS Appl Mater Interfaces* 2020;12:23968-75.
- [46] Li B, Wen H-M, Zhou W, Chen B. Porous Metal-organic frameworks for gas storage and separation: what, how, and why? *J Phys Chem Lett* 2014;5:3468-79.
- [47] Guo Z-J, Yu J, Zhang Y-Z, Zhang J, Chen Y, Wu Y, et al. Water-stable In(III)-based metal-organic frameworks with rod-shaped secondary building units: single-crystal to single-crystal transformation and selective sorption of C₂H₂ over CO₂ and CH₄. *Inorg Chem* 2017;56:2188-97.
- [48] Juan-Alcañiz J, Gielisse R, Lago AB, Ramos-Fernandez E V, Serra-Crespo P, Devic T, et al. Towards acid MOFs - catalytic performance of sulfonic acid functionalized architectures. *Catal Sci Technol* 2013;3:2311-8.
- [49] Li Y, Yang RT. Significantly enhanced hydrogen storage in metal-organic frameworks via spillover. *J Am Chem Soc* 2006;128:726-7.

- [50] Mendiratta S, Usman M, Lu K-L. Expanding the dimensions of metal-organic framework research towards dielectrics. *Coord Chem Rev* 2018;360:77-91.
- [51] Wade CR, Corrales-Sanchez T, Narayan TC, Dincă M. Postsynthetic tuning of hydrophilicity in pyrazolate MOFs to modulate water adsorption properties. *Energy Environ Sci* 2013;6:2172-7.
- [52] Ghosh P, Colón YJ, Snurr RQ. Water adsorption in UiO-66: the importance of defects. *Chem Commun* 2014;50:11329-31.
- [53] Han B, Chakraborty A. Water adsorption studies on synthesized alkali-ions doped Al-fumarate MOFs and Al-fumarate + zeolite composites for higher water uptakes and faster kinetics. *Microporous Mesoporous Mater* 2019;288:109590.
- [54] Permyakova A, Wang S, Courbon E, Nouar F, Heymans N, D'Ans P, et al. Design of salt-metal organic framework composites for seasonal heat storage applications. *J Mater Chem A* 2017;5:12889-98.
- [55] Khutia A, Rammelberg HU, Schmidt T, Henninger S, Janiak C. Water sorption cycle measurements on functionalized MIL-101Cr for heat transformation application. *Chem Mater* 2013;25:790-8.
- [56] Yan J, Yu Y, Ma C, Xiao J, Xia Q, Li Y, et al. Adsorption isotherms and kinetics of water vapor on novel adsorbents MIL-101(Cr)@GO with super-high capacity. *Appl Therm Eng* 2015;84:118-25.
- [57] Xie Y, Fang Z, Li L, Yang H, Liu T-F. Creating chemisorption sites for enhanced CO₂ photoreduction activity through alkylamine modification of MIL-101-Cr. *ACS Appl Mater Interfaces* 2019;11:27017-23.

- [58] Akiyama G, Matsuda R, Sato H, Takata M, Kitagawa S. Cellulose hydrolysis by a new porous coordination polymer decorated with sulfonic acid functional groups. *Adv Mater* 2011;23:3294-7.
- [59] Hong D-Y, Hwang YK, Serre C, Férey G, Chang J-S. Porous chromium terephthalate MIL-101 with coordinatively unsaturated sites: surface functionalization, encapsulation, sorption and catalysis. *Adv Funct Mater* 2009;19:1537-52.
- [60] Ma L, Xu L, Jiang H, Yuan X. Comparative research on three types of MIL-101(Cr)-SO₃H for esterification of cyclohexene with formic acid. *RSC Adv* 2019;9:5692-700.
- [61] Akiyama G, Matsuda R, Sato H, Hori A, Takata M, Kitagawa S. Effect of functional groups in MIL-101 on water sorption behavior. *Microporous Mesoporous Mater* 2012;157:89-93.
- [62] Bernt S, Guillermin V, Serre C, Stock N. Direct covalent post-synthetic chemical modification of Cr-MIL-101 using nitrating acid. *Chem Commun* 2011;47:2838-40.
- [63] Klinkebiel A, Reimer N, Lammert M, Stock N, Lüning U. Sulfonyl chlorides as an efficient tool for the postsynthetic modification of Cr-MIL-101-SO₃H and CAU-1-NH₂. *Chem Commun* 2014;50(66):9306-9308.
- [64] Khutia A, Janiak C. Programming MIL-101Cr for selective and enhanced CO₂ adsorption at low pressure by postsynthetic amine functionalization. *Dalton Trans* 2014;43(3):1338-1347.
- [65] Echaide-Górriz C, Aysa-Martínez Y, Navarro M, Téllez C, Coronas J. Polyamide-MIL-101(Cr) thin films synthesized on either the outer or inner surfaces of a

- polysulfone hollow fiber for water nanofiltration. *ACS Appl Mater Interfaces* 2021;13:7773-83.
- [66] Bao W, Zhang Z, Qu Y, Zhou C, Wang X, Li J. Confine sulfur in mesoporous metal-organic framework @ reduced graphene oxide for lithium sulfur battery. *J Alloys Compd* 2014;582:334-40.
- [67] Somayajulu Rallapalli PB, Raj MC, Patil D V, Prasanth KP, Somani RS, Bajaj HC. Activated carbon @ MIL-101(Cr): a potential metal-organic framework composite material for hydrogen storage. *Int J Energy Res* 2013;37:746-53.
- [68] Yanagita K, Hwang J, Shamim JA, Hsu W-L, Matsuda R, Endo A, et al. Kinetics of water vapor adsorption and desorption in MIL-101 metal-organic frameworks. *J Phys Chem C* 2019;123:387-98.
- [69] Tadros T. Adsorption isotherm BT - encyclopedia of colloid and interface science. in: Tadros T, editor., Berlin, Heidelberg: Springer Berlin Heidelberg; 2013, p. 2.
- [70] Sarce Thomann F, Hall MR, Mokaya R, Stevens LA. Hygrothermal simulation-informed design of mesoporous desiccants for optimised energy efficiency of mixed mode air conditioning systems. *J Mater Chem A* 2015;3:17290-303.
- [71] Seo Y-K, Yoon JW, Lee JS, Hwang YK, Jun C-H, Chang J-S, et al. Energy-efficient sehumidification over hierarchically porous metal-organic frameworks as advanced water adsorbents. *Adv Mater* 2012;24:806-10.
- [72] Ko N, Choi PG, Hong J, Yeo M, Sung S, Cordova KE, et al. Tailoring the water adsorption properties of MIL-101 metal-organic frameworks by partial functionalization. *J Mater Chem A* 2015;3:2057-64.

- [73] Meunier FC, Goguet A, Shekhtman S, Rooney D, Daly H. A modified commercial DRIFTS cell for kinetically relevant operando studies of heterogeneous catalytic reactions. *Appl Catal A Gen* 2008;340:196-202.
- [74] Rieth AJ, Hunter KM, Dincă M, Paesani F. Hydrogen bonding structure of confined water templated by a metal-organic framework with open metal sites. *Nat Commun* 2019;10:4771.
- [75] Hunger J, Beta IA, Böhlig H, Ling C, Jobic H, Hunger B. Adsorption structures of water in NaX studied by DRIFT spectroscopy and neutron powder diffraction. *J Phys Chem B* 2006;110:342-53.
- [76] Couble J, Gravejat P, Gaillard F, Bianchi D. Quantitative analysis of infrared spectra of adsorbed species using transmission and diffuse reflectance modes: Case study: Heats of adsorption of CO on TiO₂ and CuO/Al₂O₃. *Appl Catal A Gen* 2009;371:99-107.
- [77] Okparanma RN, Araka PP, Ayotamuno JM, Mouazen AM. Towards enhancing sustainable reuse of pre-treated drill cuttings for construction purposes by near-infrared analysis: A review. *J Civ Eng Constr Technol* 2018;9(3):19-39.
- [78] Sirita J, Phanichphant S, Meunier FC. Quantitative analysis of adsorbate concentrations by diffuse reflectance FT-IR. *Anal Chem* 2007;79:3912-8.
- [79] Berendsen HJC, Grigera JR, Straatsma TP. The missing term in effective pair potentials. *J Phys Chem* 1987;91:6269-71.
- [80] Tauler R, Brown S. *Comprehensive chemometrics: chemical and biochemical data analysis*. Elsevier Science; 2009.
- [81] Keupp J, Schmid R. Molecular dynamics simulations of the “breathing” phase transformation of MOF nanocrystallites. *Adv Theory Simulations* 2019;2:1900117.

- [82] Han SS, Choi S-H, van Duin ACT. Molecular dynamics simulations of stability of metal-organic frameworks against H₂O using the ReaxFF reactive force field. *Chem Commun* 2010;46:5713-5.
- [83] Adatoz E, Keskin S. Application of MD simulations to predict membrane properties of MOFs. *J Nanomater* 2015;2015:136867.
- [84] Dubbeldam D, Calero S, Ellis DE, Snurr RQ. RASPA: molecular simulation software for adsorption and diffusion in flexible nanoporous materials. *Mol Simul* 2016;42:81-101.
- [85] Mahoney MW, Jorgensen WL. A five-site model for liquid water and the reproduction of the density anomaly by rigid, nonpolarizable potential functions. *J Chem Phys* 2000;112:8910-22.
- [86] Stillinger FH, Rahman A. Improved simulation of liquid water by molecular dynamics. *J Chem Phys* 1974;60:1545-57.
- [87] Jorgensen WL, Chandrasekhar J, Madura JD, Impey RW, Klein ML. Comparison of simple potential functions for simulating liquid water. *J Chem Phys* 1983;79:926-35.
- [88] Zielkiewicz J. Structural properties of water: Comparison of the SPC, SPCE, TIP4P, and TIP5P models of water. *J Chem Phys* 2005;123:104501.
- [89] Alabarse FG, Haines J, Cambon O, Levelut C, Bourgogne D, Haidoux A, et al. Freezing of water confined at the nanoscale. *Phys Rev Lett* 2012;109:35701.
- [90] Hernández de la Peña L, Kusalik PG. Quantum effects in liquid water and ice: Model dependence. *J Chem Phys* 2006;125:54512.
- [91] Chau P-L, Hardwick AJ. A new order parameter for tetrahedral configurations. *Mol Phys* 1998;93:511-8.

- [92] Yamashita K, Daiguji H. Molecular simulations of water adsorbed on mesoporous silica thin films. *J Phys Chem C* 2013;117:2084-95.
- [93] Meier K, Laesecke A, Kabelac S. Transport coefficients of the Lennard-Jones model fluid. II Self-diffusion. *J Chem Phys* 2004;121:9526-35.
- [94] Johnson SG, Frigo M. A modified split-radix FFT with fewer arithmetic operations. *IEEE Trans Signal Process* 2007;55:111-9.
- [95] Miyazaki M, Fujii A, Ebata T, Mikami N. Infrared spectroscopic evidence for protonated water clusters forming nanoscale cages. *Science* (80-) 2004;304:1134 LP - 1137.
- [96] Martí J, Gordillo MC. Effects of confinement on the vibrational spectra of liquid water adsorbed in carbon nanotubes. *Phys Rev B* 2001;63:165430.
- [97] Fröhlich D, Pantatosaki E, Kolokathis PD, Markey K, Reinsch H, Baumgartner M, et al. Water adsorption behaviour of CAU-10-H: a thorough investigation of its structure-property relationships. *J Mater Chem A* 2016;4:11859-69.
- [98] Yada H, Nagai M, Tanaka K. The intermolecular stretching vibration mode in water isotopes investigated with broadband terahertz time-domain spectroscopy. *Chem Phys Lett* 2009;473:279-83.
- [99] Dalla Bernardina S, Paineau E, Brubach J-B, Judeinstein P, Rouzière S, Launois P, et al. Water in carbon nanotubes: the peculiar hydrogen bond network revealed by infrared spectroscopy. *J Am Chem Soc* 2016;138:10437-43.
- [100] Brubach J-B, Mermet A, Filabozzi A, Gerschel A, Roy P. Signatures of the hydrogen bonding in the infrared bands of water. *J Chem Phys* 2005;122:184509.
- [101] Cmglee. Water Phase diagram. https://en.wikipedia.org/wiki/Phase_diagram.

- [102] Yanagita K. Water adsorption capacity of metal organic frameworks. University of Tokyo, 2018.
- [103] Chiashi S, Saito Y, Kato T, Konabe S, Okada S, Yamamoto T, et al. Confinement effect of sub-nanometer difference on melting point of ice-nanotubes masured by photoluminescence spectroscopy. ACS Nano 2019;13:1177-82.
- [104] Morishige K, Uematsu H. The proper structure of cubic ice confined in mesopores. J Chem Phys 2005;122:44711.